Temperature Control System Design for Flame-Sprayed Coating Based Heating Systems

by

Jacob Maxwell John

A thesis submitted in partial fulfillment of the requirements for the degree of

Master of Science

Department of Mechanical Engineering
University of Alberta

Abstract

A 2 cm thick American Iron and Steel Institute (AISI) 1018 steel sample was flame-sprayed with Alumina (Al_2O_3) then a metal matrix composite consisting of Nickel-Chromium-Aluminum-Yttrium (NiCrAlY) and Alumina split 50 % by weight. A first order transfer function was derived from a lumped capacity model and was used to define parameters: time constant and gain which describe the dynamics of the heating system. Step inputs of 3, 6, and 9 V were applied to the heating element under internal forced convection heating conditions at an air temperature controlled to 15 °C. Temperature measurements were used to determine time constant, zero frequency gain, and confirm the Biot assumption. Heat transfer coefficient (HTC) dictating convective heat transfer rate was predicted from experimental measurements using the lumped capacity governing equation and a finite difference to describe the time derivative, values ranged from 208 W/m^{2}K and 250 W/m^{2}K. Experimental HTC was compared to theoretical HTC predictions showing a 40 % to 58 % difference. The resistance to temperature relationship for the coating material was measured using two voltage dividers in series. Results showed a maximum 2 % change in resistance over the experiment. Measured values were used in transfer function simulations to verify against experimental results, this showed that the linear model effectively predicts the non-linear system within the tested operating range. A sensitivity study shows the affect of uncertain parameters on transfer function predictions. Low uncertainty parameters are: area of the coated surface, density, thermal heat capacity, and thickness of the steel sample. High uncertainty parameters are: HTC and resistance across the flame sprayed Joule-heating element. After the transfer function was

verified experimentally, it was used to design a temperature control system including a PI (Proportional integral) controller with windup control and input saturation management to provide a robust and energy efficient response.

Preface

This thesis is an original work by Jacob Maxwell John. Some of the thesis was previously published for the ITSC 2020 Conference. Due to the 2020 pandemic attendance of the conference was not possible.

In memory of the people who lost their lives in flight 752. Our community lost friends, colleagues, and in some cases family. The loss will not be forgotten.

Acknowledgements

I send gratitude to my supervisors Dr. André McDonald and Dr. Hossein Rouhani. They provided the framework for disciplined research.

I am in debt to Dr. McDonald for providing me with the opportunity to do this work. He supported my development as a professional by pushing me towards my goals, supporting the attendance to important developmental events, and is a role model to me in taking initiative towards high aspirations. His organized and disciplined approach to manufacturing will stay with me.

Dr. Rouhani's experience in control system design guided me towards useful results. He met my ideas with understanding and practicality. Also, his patience supported my growth during this developmental period.

Appreciation the staff at the University of Alberta. Rick Conrad for his advice on electric component design. The machine shop staff for what they taught me. The staff, and users, at the engineering garage who shared lessons from their mistakes.

Thanks must be sent to my friends, who made my graduate experience unforgettable. Special thanks to Jerry Han and Daniel Aldrich. Jerry for the late evenings we shared studying/collaborating, and the discussions in which we question important assumptions. Daniel, for the LaTeX template I used to create my thesis.

In the end, I thank my family and friends who have encouraged me to pursue an education in engineering. I will use what I have learned to benefit as many as possible and pay back my debt to society.

Table of Contents

List of Tables

List of Figures

List of Symbols

Latin

$\dot{\triangle}E$	Rate of change of energy inside the coated sample control volume
$\dot{\triangle}E_{\text{in}}$	Rate of energy entering coated sample control volume
$\dot{\triangle}E_{\text{out}}$	Rate of energy leaving coated sample control volume
$\frac{dT}{dt}$	Rate of change of the bulk temperature of the coated steel sample with respect to time
$\overline{V}^2(s)$	Laplace Transform of input to transfer function (Voltage squared)
Bi	Biot Number
Nu_1	Nusselt number for case 1
Nu_2	Nusselt number for case 2
Nu_3	Nusselt number for case 3
Nu	Nusselt number
$\text{Re}_{\text{D}_{\text{h1}}}$	Reynold's number inside the duct case 1
$\text{Re}_{\text{D}_{\text{h2}}}$	Reynold's number inside the duct case 2
$\text{Re}_{\text{D}_{\text{h3}}}$	Reynold's number inside the duct case 3
$\text{Re}_{\text{D}_{\text{h}}}$	Reynold's number inside the duct
τ	Time constant
$\boldsymbol{x}$	Dimension in x direction of Cartesian coordinate system

$\boldsymbol{y}$ Dimension in y direction of Cartesian coordinate system

$\boldsymbol{z}$ Dimension in z direction of Cartesian coordinate system

A Surface area of coated sample exposed to convective heat transfer

a Width of duct

A_{coating} Cross section of coating

A_{duct} Cross sectional area of the forced air apparatus

b Height of duct

c Thermal heat capacity of the coated sample

$C(s)$ Controller transfer function in s domain

D Thickness of coating

d Discrete step size

D_{h} Hydraulic diameter

$G(s)$ Plant/controller open loop transfer function in s domain

H Height of sample in z-direction

$h(m)$ Discrete heat transfer coefficient

$H(s)$ Plant/controller closed loop transfer function in s domain

$h(t)$ *or* h Continuous time heat transfer coefficient

h_{nominal} Nominal value for heat transfer coefficient for sensitivity study

I Current passing through shunt resistor and sample

I_1 Current through first voltage divider

I_2 Current through shunt resistor

I_3 Current through sample

I_4 Current through second voltage divider

I_{total} Total current supplied to sample, shunt resistor, and voltage dividers

K Zero order gain

k Thermal conductivity of coated sample

$k(T_{\text{f}})$ Thermal conductivity of air at film temperature

K_{d} Derivative gain

K_{i} Integral gain

K_{p} Proportional gain

L Length of sample in x-direction

l Length of sample perpendicular to flow

$L_{\text{h, turbulent}}$ Hydrodynamic length

m Discrete time index

p Perimeter of the cross sectional area of the forced air apparatus

$P(s)$ Plant transfer function in s domain

$R1,\ R2,\ R3,\ R4$ Resistances for resistors in positions 1 through 4

R_{coating} *or* R Resistance across copper terminals of coated sample

R_{nominal} Nominal value for coating resistance for sensitivity study

R_{shunt} Shunt resistor value

s s variable including frequency and time decay

t time

$T(m)$ Discrete bulk temperature of coated sample

$T(R)$ Temperature as a function of resistance correlation for coating material

$T(t)$ Bulk temperature of coated sample in continuous time

T_{f} Film temperature along the surface of the heated sample

$T_{\text{inf}}(m)$ Discrete environment temperature inside cold room

T_{inf} *or* T_{air} Environment temperature inside the cold room

T_{i} Initial bulk temperature of sample

T_{sur} Surface temperature of coated steel block

V Potential difference driving current through the coated heating element

$V1$ Voltage difference between node A and D

$V2$ Voltage difference between node B and C

V_{avg} Average velocity of flow through forced air apparatus

V_{sig1} Voltage signal received by micro-controller from first voltage divider

V_{sig2} Voltage signal received by micro-controller from second voltage divider

W Width of sample in y-direction

$X(z)$ z transform of the input from filter transfer function

$Y(z)$ z transform of the output from filter transfer function

z Complex variable z including frequency component and time decay

Greek

ν Kinematic viscosity of air inside the duct

$\overline{\theta}(s)$ Laplace transform of output of transfer function (temperature increase)

ρ Density of coated sample

$\theta(t)$ Temperature increase with respect to initial temperature

$\varrho(T)$ Resistivity of coating material as a function of bulk temperature

ϱ Resistivity of coating material

Abbreviations

AISI American Iron and Steel Institute.

APS Atmospheric Plasma Spray.

CFD Computational Fluid Dynamics.

CNC Computer Numerical Control.

FAA Federal Aviation Administration.

FBD Free Body Diagram.

FIR Finite Impulse Response.

FMR Flow Monitor Reading.

FRPC Fiber Reinforced Polymer Composite.

HTC Heat Transfer Coefficient.

HVOF High Velocity Oxy-Fuel.

ILC Iterative Learning Control.

LQR Linear Quadratic Regulator.

MMC Metal Matrix Composite.

NASA National Aeronautics and Space Administration.

PCB Printed Circuit Board.

PI Proportional Integral.

PID Proportional Integral Derivative.

SEM Scanning Electron Microscope.

SPS Suspension Plasma Spray.

SST Steady State Temperature.

UAV Unmanned Aarial Vehicle.

VPS Vacuum Plasma Spray.

WWII World War II.

Chapter 1

Introduction

1.1 Ice Accretion

Ice accretion on structures in cold environments from moisture in the atmosphere creates significant concern in aviation and wind energy production industries. Wind energy is the fastest growing form of energy production and it is common to use flying machines. Ice layers interfere with carefully designed aerodynamic surfaces resulting in losses in lift performance and increased drag. Icing research began in the early 1930's, but not until WWII were the first icing tunnels built in the war effort [1]. In 1979 the National Aeronautics and Space Administration (NASA) aircraft-icing program was initiated, and Computational Fluid Dynamics (CFD) was applied to the prediction of aerodynamic performance of airfoils with ice accretions. With the advances in manufacturing and computing, opportunities exist for scientists and engineers to attempt to solve this long lasting problem.

1.1.1 Effects of Ice Accretion on Aircraft and Wind Turbine Performance

Depending on the geometry of the airfoil [2] and style of ice accumulation [1], this phenomenon can reduce lift by as much as 30 % and increase drag by more than 50 % [2, 3]. Tests performed on an aircraft wing with an aspect ratio of 6 show a 25 % reduction in maximum lift and a 90 % increase in drag for the conditions tested

[4]. Ice can render aircraft unsuitable for flight and even cause catastrophic failure. Icing events are responsible for approximately 9 % of significant safety accidents of aircraft [5]. Between the years of 1998 and 2007, 1049 icing-related accidents in large and small aircraft were reported to the Federal Aviation Administration (FAA) and NASA [6]. From 1975 to 1988, 803 icing accidents occurred in the United States and approximately half resulted in fatalities [7]. Ice is heavy, it increases pressure and skin drag, and can impede the motion of control surfaces used to steer and balance the machine. This is a problem which exists for all flying machines, from small unmanned aircraft [8] to commercial airliners. Further, dislodged ice can damage the aircraft skin, antennas, other instrumentation, ice can even disable or destroy engines if ingested. For helicopters, ice shedding can cause a rotating imbalance, resulting in severe vibration and difficulty to control [9].

Field measurements show that ice formation can reduce annual energy production for wind turbines by up to 17 % depending on altitude and atmospheric conditions [10]. From simulations, icing is predicted to reduce power production from wind turbines by more than 20 % [11], this prediction was made for rime-ice accretion. Aside from power losses, icing of wind turbine blades also provides concerns in terms of safety through the mechanisms of ice-throw [12] and fatigue loading [13]. The substantial mass of ice and forces from aerodynamic imbalances on rotating equipment cause stress fluctuations, and can result in failure.

1.1.2 Fundamentals of Ice Accretion

Warm air can contain more water than an equivalent mass of cold air. When moist warm air mixes with cold air, the relative humidity of air rises. Condensation on solid particles or surfaces occurs at 100 % relative humidity, resulting in icing conditions if air temperature is below 0 °C. Elevation also increases risk of icing. Elevation increase is proportional to air pressure decrease, and water vapor saturation decrease. This is why precipitation occurs high in the atmosphere. Further, dry air is more dense then

wet air at the same temperature. The density of dry air at 20 °C (1 atm) is 1.204 $\frac{kg}{m^3}$ [14] and the density of wet air at 20 °C (1 atm) is 1.199 $\frac{kg}{m^3}$[15], for reference the density of dry air at -25 °C (1 atm) is 1.422 $\frac{kg}{m^3}$. Air is mostly composed of diatomic Nitrogen (N_2) and diatomic oxygen (O_2), each having atomic masses of 28 and 32 respectively. The atomic mass of water (H_2O) is 18. Water molecules are weakly attracted to each other, resulting from their polarity [16]. This has a negligible affect on the density of wet air. Density differences of air drive mixing on at atmospheric scale, and carry moisture into the atmosphere where ice accretion on airplanes, wind turbines, bridges, and many other man-made structures occurs.

Table 1.1: Ice Formation [17]

	Rime	Glaze
Liquid Water Content	Low	High
Air Temperature	Low	Near Freezing
Flight Velocity	Low	High
Freezing Fraction	One	Less Than One
Droplets Freeze	On Impact	Flow On Surface
Ice Color	White, Opaque	Clear
Ice Density	$<$ 1 gm/cc	1 gm/cc

High levels of humidity combined with frequent changes of passing cold and warm fronts result in high risk icing conditions [18]. There are three main type of ice formation: in-cloud icing, precipitation icing, and hoar frost. Hoar frost is a direct phase transition from vapor in the air to solid ice on a surface, often with negligible thickness. Rime and glaze ice pertain to impingement of super-cooled water droplets upon a surface followed by a phase transition from liquid to solid [17]. The phase transition may occur immediately resulting in soft rime or hard rime ice, or it may

happen gradually resulting in glaze ice [19]. Rime ice is seen at lower temperatures -40 °C to -10 °C, while glaze ice is seen at higher temperatures -18 °C to -0 °C [9].

Conditions to form rime and glaze ice are identified in Table 1.1, this figure is from Bragg's 1981 PhD dissertation on ice formation. Formation of rime ice commonly occurs on smaller aircraft flying through a cloud. It can be identified as a opaque ice layer extending into the oncoming air stream [17]. Rime ice is opaque, because it freezes quickly and entraps air between ice crystals. Rime ice essentially acts as an extension to the airfoil, but with much higher surface roughness resulting in an early boundary layer transition [9]. Glaze ice is more common on transport jets flying through precipitation conditions. Glaze ice can be identified as a clear layer with a horn shape [17]. Researchers have further classified structure of ice formations since Bragg's work [20].

1.2 Ice Accretion Mitigation

In his 1981 dissertation [17], Bragg describes why the icing problem is such a challenge. Avoiding icing by remaining on the ground during icing conditions is not a solution easily accepted. Atmospheric conditions and physical processes cause the icing problem, as a result the solutions are very complex and are often tailored to the application. In 1981, he states that the installation of mechanical or thermal ice mitigation systems commonly occur as a retrofit or add-on to an aircraft.

Ice mitigation techniques consist of deicing and anti-icing systems. Ice mitigation systems often employ both a deicing technology and an anti-icing technology. Economics or engineering redundancy can be justification for such systems. Deicing refers to systems that eliminate ice buildup after accretion has occurred, whereas anti-icing systems impede ice accretion. Provided the compelling reasons to develop ice mitigation systems, many people have attempted to solve the problem and a landscape of ice mitigation technologies resulted. Solutions consist of the application of mechanics, thermodynamics, and chemical science to eliminate the detrimental effects

of ice accretion on airfoils. Existing solutions are expensive, can be harmful to the environment, impede aircraft performance and safety, or reduce the efficiency of the flying machine.

In recent years, electro-thermal systems have been of interest [21]. Electro-thermal systems can be automated, they require low power, do not impede the performance of engines, reliably eliminate the concern of ice accretion, and promise favorable economics. The automation of electro-thermal systems requires that two main problems are addressed: the detection of accreted ice and the thermal control of the heat generating surface.

1.2.1 Passive Ice Mitigation (Anti-Icing)

Application of freezing point depressants [9] is the most common ice mitigation technique for airplanes today. Ethylene glycol was first used in WWII by British engineers to prevent buildup of ice on the wings of a Cessna 206 [9]. The fluid would bleed out of stainless steel pores fitted to the leading edge of the airfoil using rivets. The fluid was used to keep leading edges, propeller blades, and windshield clear of ice. Airplane anti-icing fluids can leave residue in critical areas in the wings and stabilizers of aircraft. The residue can rehydrate, expand into a gel material, and freeze, restricting the flight control system [22]. This anti-icing technique requires that operators of aircraft are inspecting for the buildup, and planning for the removal of this residue. This results in operational delays. Also, application of these chemicals is harmful to the environment and can result in delays.

Superhydrophobic coatings were tested in [23]. The coatings effectively reduce the adhesion strength of ice to the surface, but the anti-icing properties of the coating deteriorate with de-icing cycles as surface asperities gradually break [23]. It was also found that the anti-icing efficiency of the tested superhydrophobic surfaces was significantly lower in a humid atmosphere. Ice formed above and below the surface asperities, implying that superhydrohobic coatings may not always be ice-phobic.

1.2.2 Active Ice Mitigation (Deicing)

Thermal energy reliably eliminates ice. The most prevalent method of delivering thermal energy to accreted ice layers on airfoils are bleed air systems. Bleed air systems redirect hot compressed air from turbojet or turboprop engines in veins located behind the leading edge of a wing. For piston driven engines, waste heat is recaptured, and a fuel-burning combustion heater is used to further heat the air. These systems are effective at eliminating ice buildup, but reduce the efficiency of the engines or consume fuel that would otherwise be used to propel flight [9].

To reduce the amount of energy required to remove ice, surface deformation is applied [9]. Three deformation systems have been researched.

1. Pneumatic boots

2. Electromagnetic impulse deicing

3. Electromagnetic expulsive boots

The pneumatic boot technology is the most common, and is used in general aviation. Since ice accretion must occur prior to the actuation of such a system, a certain amount of drag rise and lift loss is inevitable with this system. The pneumatic boot is an inflatable bladder. The surface deforms when the boot is engaged, ice cracks, and aerodynamic forces remove ice from the surface. The video [24] shows pneumatic boots operating. A number of pressure cycles are engaged, but the ice is not entirely removed from the leading edge.

For a small Unmanned Aerial Vehicles (UAV) deicing system, Sorensen used Carbo e-therm PUR-120 1W as a conductive coating to generate heat [8, 25, 26]. This material is a carbon based low-viscosity liquid. Resistance of the strip is proportional to layer thickness, width, and length. Sabatier *et al.* applied a conductive paint covered with a coating of gel for protection [27]. This was found to be an effective

solution for the application, but would not meet durability requirements for deicing large aircraft.

For wind turbines, many active and passive methods are in development, but few are available on the market. Active heating of wind turbine blades, similar to the bleed air system for aircraft, is the most tested. Active heating systems are used in combination with hydrophobic coatings to reduce power consumption of the deicing system [19].

1.2.3 Ice Detection

Is his dissertation, K. Sorensen analyzed the aerodynamics of unmanned UAV during flight to determine the presence of ice [25]. Changes in lift and drag coefficient were correlated to ice accretion on the air frame. At a 10 % decrease in lift and 10 % increase in drag, the system raises an alert for the presence of ice. While this method works for small UAV, making the measurements required to apply this model on larger aircraft may not be practical. Other researchers have worked to apply machine learning to ultrasonic sensor data [28] to detect the presence of ice on wind turbine blades. Anemometers in combination with relative humidity sensors can be used to provide reliable, and affordable, ice detection for wind turbines [19]. Power curve analysis is also a reliable method to detect ice on wind turbine blades [19]. More researchers have applied Kalman filters and neural networks to aircraft dynamics [29, 30] to statistically detect ice accretion on air-frames.

1.2.4 Thermal Control

Once ice is detected, the temperature control of the airfoil surface is what eliminates accreted layers of ice. PID (Proportional Integrator Derivative) control can be used to solve this problem, and gains can be tuned to closely meet desired performance [8, 25]. PID control provides ease of implementation, but does not enable refinement of plant dynamics. PID control can be implemented without a model, since the method

employs an error signal, and gains, to determine the magnitude of the input to the plant. An error signal is generated by taking the difference between a measured state and a specified set-point. This controller is simple to implement because only sensors and a micro-controller are required for successful operation. A model of the plant is useful to simulate dynamics including the controller, and thus specify gains prior to operation of the system. PID controllers operate on current and past state information, and do not include a model predicting plant behavior. This can lead to overshooting a set-point as result of built up numerical error if the input actuator is saturated. Also, gain parameters remain constant so the dynamics of such a system are not optimal. To ensure all locations on a surface for deicing are warm enough, Sabatier implemented temperature feedback from a location on the airfoil predicted to be furthest from the desired set point [27].

Control methods employing a model are helpful for achieving optimal control, setting input/output limits, and making sensor-less predictions of a state. The designer of an electro-thermal ice mitigation system should use a model to implement Linear Quadratic Regulator (LQR) control in order to determine a cost function used to optimize the system for either speed or efficiency [30].

1.3 Thermal Spray for Joule (Resistive) Heating

Thermal coatings provide desirable characteristics for joule heating elements. Thermal coatings are robust, they can effectively resist erosion, corrosion, and mechanical damage since the coating can be constructed from some of the hardest metals and ceramics available to industry. Titanium carbide (TiC) or Alumina (Al_2O_3) are some examples of hard coating materials. High Velocity Oxy-Fuel (HVOF), Vacuum Plasma Spray (VPS), Plasma Spray, and Flame Spray [31–33] thermal coating technologies have been examined by researchers for the construction of resistive heating elements.

Tejero-Martin *et al.* [34] recently published an extensive review of thermal coating

technologies and some applications. This document is referenced to describe these advanced manufacturing techniques. What all thermal spray technologies have in common is the use of kinetic and thermal energy to melt (or partially melt) metallic (or non-metallic) particles in order to coat machine parts with exotic materials with impressive mechanical, chemical, thermal, or electrical properties. The choice of thermal coating technology depends on the application. Thermal coatings have become an essential part of today's industry.

1.3.1 Flame Spray

Flame spray was invented in 1909, and was the first thermal spray technique devised. Pressurized combustible gasses, such as mixed streams of Oxygen (O_2) and Acetylene (C_2H_2) are ignited and used to accelerate particles toward a surface. Effectively coating a part. Flame temperatures for this technique are around 3,000 K and particle velocities are around 100 m/s.

1.3.2 High Velocity Oxy-Fuel (HVOF)

This technique is an innovation upon flame spray, and the concept is similar to a jet engine. Gasses are ignited inside a combustion chamber, producing high pressures. Gasses exit through a nozzle to produce a supersonic jet. Flame temperatures are around 3,000 K, but particle speeds can be as high as 1,000 m/s. Coatings produced with HVOF exhibit lower porosity and enhanced adherence than conventional flame sprayed coatings.

1.3.3 Atmospheric Plasma Spray (APS)

High voltages are used to produce arcs across electrodes to produce plasma from an inert gas. Pressure is generated during the rapid expansion of the inert gas as it ionized. The production of plasma heats and accelerates powdered particles. The process of producing plasma (ripping diatomic inert gas molecules apart) is aggressive

and emits a tremendous amount of energy. For this reason, plasma-flame temperatures range from 8,000 K to 14,000 K. Particle speeds range from 20 m/s to 500 m/s. These plasma-flame conditions produce coatings that can surpass the quality of flame sprayed coatings.

1.3.4 Suspension Plasma Spray (SPS)

The high temperatures of plasma flames impart thermal energy very quickly, but the energy density of the flame dissipates quickly as well. As a result, APS benefits from greater flow control of the powder feed. This limits APS to larger powder particles (10 μm to 100 μm). SPS can be used to overcome this shortfall, permitting the application of powder particles in the nano-scale. In this process the powder particles are suspended in a solution, providing greater flow control. This technique increases the complexity and cost of the process, while producing very low porosity and high density/adherence strength. In the application of thermal barrier coatings, SPS can produce coatings with lower thermal conductivity than the electron beam physical vapor deposition process.

1.3.5 Vacuum Plasma Spray (VPS)

Vacuum plasma spray was invented to further improve the quality of plasma spray coatings. By evacuating (or partially evacuating) the volume containing the plasma spray gun and the sample being coated, risk of oxidation of molten particles is eliminated (or reduced) resulting in higher coating quality. Air pressures for low pressure plasma spray range from 4,000 Pa to 40,000 Pa. Vacuum plasma spray is performed in a volume of 100 Pa air pressure or lower.

1.3.6 Benefits of Flame Spray

As the first thermal spray technique invented, flame spray is the least complex and as a result most affordable thermal spray technique. If the needs of a thermal spray

application can be met with flame spray, the case to use a more expensive spray technique is weak. More complex techniques require high voltages, vacuum systems, or expensive powder solutions. These factors significantly increase cost, and reduce the feasibility of the application being examined. Consumables for flame spray are acetylene gas, oxygen, and dry powder. An article published on March 13th, 2020 [35] states that "the global thermal spray material market was valued at USD 1,621.10 million by revenue, in 2019, and it is anticipated to reach USD 2,564 million by 2023". This market growth is fueled by "growing thermal spray applications in the automotive sector, increased usage of thermal spray in medical devices, rising popularity of thermal spray ceramic coatings, and growing applications in the aerospace and defense sector".

For this work to remain a useful competitive contribution to the market growth of thermal spray, it is important to take into consideration economic factors. Since this work can be accomplished with flame spray, flame spray was used.

1.3.7 Limitations of Flame Spray

Heat deposition is a concern when coating with flame spray. The relatively low flame temperature requires that powder particles linger in the flame for a greater period relative to thermal spray technologies that employ greater flame temperatures. Also, flame spray benefits from reduced stand off distances between the sample and the torch nozzle. This reduces the amount of time airborne powder particles have to cool, but heats the sample more. Composite materials, thin parts, or metals with low melting points can melt or significantly deform, or be destroyed, during the coating process. For applications in aerospace, this is a concern since delicate materials are common in this industry.

Successfully flame spraying an Fiber Reinforced Polymer Composite (FRPC) sample with NiCrAlY required garnet sand used as insulation between the sample and coating [33]. FRPC was successfully coated with $Al_2O_3 - 13\%TiO_3$ using APS with-

out insulation [36]. The higher flame temperature with the APS process imparts enough thermal energy to melt powder particles in a shorter distance. This permits a greater stand-off distance during the coating process, thus reducing the likelihood of melting, deforming, or destroying the sample.

An option to utilize flame spray for the construction of deicing elements is to fabricate the heating element prior to installation to the airfoil. The concept is essentially using flame spray as a 3-D additive manufacturing process. With a mold representing the shape of the airfoil, and a method to remove the constructed flame sprayed layer from the surface of the mold, heating elements could be constructed at a facility then installed to an airfoil without running the risk of damaging the surface of the airfoil.

1.3.8 Materials Examined for Flame Spray Heating Elements

The coating selection for this study was based on previous work done by the thermal spray research group at the University of Alberta. NiCrAlY on FRPC coated with garnet sand was analyzed as a heating element in [33]. NiCr 50%/50% and NiCrAlY as heating elements on steel pipe coated with Al_2O_3 was examined in [37]. The heating performance of NiCrAlY, NiCrAlY $-$ Al_2O_3 50%/50%, NiCrAlY $-$ TiO_2 50%/50%, and NiCrAlY $-$ WC/12Co 50%/50% were compared using standardized steel samples coated with Al_2O_3 [38]. The heating performance of FeCrAlY as a heating element on a titanium sample coated with Al_2O_3 is analyzed in [39].

In this work, NiCrAlY $-$ Al_2O_3 50%/50% was selected for its high resistivity and weak relationship between temperature and resistance. The high resistivity of the coating material makes it easier to achieve desirable resistance values across power terminals of the sample. The weak relationship between resistance and temperature reduce the uncertain parameters when verifying the transfer function. Depending on the application of the coating, it may be desirable to have a strong relationship between temperature and resistance.

1.3.9 Smart Thermal Coatings

Thermal coatings are typically used to enhance mechanical or chemical surface properties of an object. Smart coatings either respond to, or collect information from their environment. A sensor developed with a thermal coating technology enhances mechanical properties of the surface, while providing a source of information. A thermal coating which acts as a sensor has applications in industries where other sensor technologies cannot safely operate. In his PhD dissertation R. Henriquez applied $Al-12Si$ to an FRPC structure for damage detection [40]. The effect of damage to the FRPC on the coating was characterized, and can be used to predict damage done to FRPC structures. Smart overlay coatings provide high temperature corrosion protection over a wide range of operating conditions [41]. The chemical makeup of the coating responds accordingly to the operating condition. The solar absorbing properties of Ni-Mo based thermal spray coatings were enhanced with laser treatment [42], a potential application for this is to reduce energy consumption of coating based heating systems.

This thesis examines a smart coating application: using thermal spray to generate heat and provide feedback to a controller for making operational decisions. Given the scarcity of publications on smart coatings, and particularly on using coatings in control systems, further study is needed in this field.

1.4 Motivations

The motivation of this work is to explore the temperature control system design of flame sprayed heating elements. This is motivated by the lack of control system design discussion in the field of flame sprayed heating elements. A transfer function describing the temperature response to a voltage input is derived and verified using engineering practice. The function was then used to simulate the response of a system controlled with a PI controller. This work leaves open the opportunity to

develop advanced control systems for more efficient, and robust, control of electro-thermal heating systems for industrial application in anti-icing/deicing systems in aviation and wind power production industries. Throughout this work, the application of techniques, and methods, used to verify the transfer function are explored and discussed.

1.5 Objectives

The objective of this work is to design a control system to regulate temperature of a flame sprayed heating element. In order to achieve this goal, a transfer function was derived. Verification was required. A first-order lumped capacity model was used to describe the temperature response of the coated sample to voltage input. Experiments were conducted to investigate the validity of this model, determine if this linear model can be used to approximate the non-linear behavior of the thermal system, and specify how the geometry and material properties of the coating, and sample, effect the dynamics of the heating system. The following studies were performed in order to verify the model and proceed with control system design.

1. Forced convection heating experiments to compare predicted results to experimental results. Experimental determination of HTC was required, in addition to theoretical determination of HTC.

2. Resistance to Temperature characterization of the coating in order to determine the affect of resistance change on experimental temperature measurements. This required design and fabrication of an appropriate resistance sensor.

3. Verify the Biot assumption used to simplify the model to lumped capacity. A steel sample was used. If the model is valid for a steel sample it is also valid for an aluminum sample with the same dimensions. Steel has a relatively low thermal conductivity 10 - 61 $\frac{\mathrm{W}}{\mathrm{mK}}$ [43] dependent on alloy type. 52 $\frac{\mathrm{W}}{\mathrm{mK}}$ for 1018

AISI steel in this study. By verifying the model with steel, the model can be applied to applications considering other materials.

4. Perform a sensitivity study to examine the effect which non-linear changes of HTC have on the output of the the transfer function. Also, to examine the effect which resistance change has on transfer function predictions.

The results from this study were used to design a control system for regulation of temperature using flame sprayed heating elements. Also, future work for the improvement of such systems was discussed.

1.6 Thesis Organization

This thesis is organized into chapters describing the process followed in order to achieve the goals of this study. Chapter 2 discusses the theoretical derivation of the lumped capacity model, theoretical predictions of HTC, and summarizes any design that was required in order to construct the flame sprayed sample and resistance sensor. Chapter 3 discusses the fabrication of designed components and the experimental process to collect reliable results. Chapter 4 describes the analysis performed with the collected data, discusses observations of nuances in the data, and summarizes the control system design in order to complete this work. Chapter 5 states the conclusions from this work and suggests work for future students or control system engineers. Finally, the appendices contain MATLAB® code and documents used during the design and manufacturing of components for the completion of this work.

Chapter 2

Theory and Design

2.1 Assumptions and Thermal Diagram

(a) Top View (b) Side View

Figure 2.1: Thermal Free Body Diagram (FBD) Showing Dimensions and Heat Transfer Conditions

A 2 cm thick, 5 cm wide, 13.8 cm long sample of AISI 1018 steel was coated on one side with and insulating layer of Alumina then a conductive metal matrix composite (MMC) layer to act as the Joule heating element. Figure 2.1 communicates how the heating conditions for the sample under internal forced convection were interpreted. The bottom and all edges were treated as insulated. Only on the top surface, at 2.0 cm along the $\boldsymbol{z}$-axis in Figure 2.1, does heat transfer occur. Five assumptions were made in order to reduce the complexity of the problem to permit modeling the temperature distribution within the bulk material using lumped capacity.

1. Insulated ends at $\boldsymbol{x}$=0, $\boldsymbol{x}$=L, $\boldsymbol{y}$=0, and $\boldsymbol{y}$=W according to fig. 2.1
2. Bi $= \frac{h(t)H}{k} << 0.1$
3. Insulated base at $\boldsymbol{z}$=0. The sample is placed on wood

4. Heat loss to radiation is negligible. Maximum temperature expected is no more than 50 °C

5. Heat generation from resistive heating is uniform and thermal contact resistance is negligible.

2.2 Transfer Function Derivation and Parameter Definition

These assumptions imply that the temperature distribution within the sample is negligible. The first assumption eliminates temperature variation across the width and length of the sample while the second and third assumptions eliminate temperature variations across the thickness of the sample. Thus, the temperature of any point within the sample is proportional to the energy which has entered the control volume minus the energy which has left the control volume. These assumptions greatly reduce the complexity of the problem, and require consideration when looking to apply the model.

For the case of retrofitted deicing elements, the accuracy of these assumptions can be maintained by placing an insulating material between the deicing element and the surface of the airfoil. In this case, material of the deicing element is treated with lumped capacity, and a substrate does not exist.

- Assumption 1 is maintained since the thickness of such an element is low and flame spray materials can be selected such that thermal conductivity confirms the Biot assumption. The high thermal conductivity of the coating material would both confirm the Biot assumption and reduce the actual temperature distribution across the heating element.

- Assumption 2 is maintained because the area of the edges (yz and xz planes) are negligible relative to the surface area of the coating (xy plane). Thus, heat

loss at the edges ($\boldsymbol{x}$=0, $\boldsymbol{x}$=L, $\boldsymbol{y}$=0, and $\boldsymbol{y}$=W) is negligible to that of heat loss at the surface ($\boldsymbol{z}$=H).

- Assumption 3 is maintained because the element could be placed on an insulated surface.
- Assumption 4 is maintained because heat loss from convection is large relative to radiation.
- Assumption 5 can be maintained with precise control over thickness of the coating during the fabrication process in combination with an accurate understanding of the resistivity of the coating material.

In further applications where the coating is applied directly to an object, consideration of the Biot assumption and geometry of the object is important. In this study, a 2 cm thick block of steel is used to confirm the model. As heat transfer coefficient increases, thermal conductivity of the bulk material decreases, or thickness of the bulk material increases, the Biot assumption becomes increasingly less valid. Thus, application of the lumped capacitance model must be done with care.

$$\dot{\triangle}E_{\text{in}} - \dot{\triangle}E_{\text{out}} = \dot{\triangle}E \tag{2.1}$$

Energy in comes from resistive heating:

$$\dot{\triangle}E_{\text{in}} = V^2/R_{\text{coating}} \tag{2.2}$$

Energy out is from convective losses:

$$\dot{\triangle}E_{\text{out}} = hA(T(t) - T_{\text{inf}}) \tag{2.3}$$

Changes of temperature are proportional to change of energy in the control volume:

$$\dot{\triangle}E = \rho cAH * \frac{dT}{dt} \tag{2.4}$$

Resulting in the governing equation:

$$V^2/R_{\text{coating}} - h(t)A * (T(t) - T_{\text{inf}}) = \rho cAH\frac{dT}{dt} \tag{2.5}$$

Normalizing the temperature term in 2.5:

$$\theta(t) = T(t) - T_{\text{inf}} \tag{2.6}$$

Applying Laplace Transform to Equation (2.5) allows arranging the equation for output, $\theta(t)$, over input, V^2. This results in the following first order transfer function:

$$P(s) = \frac{\overline{\theta}(s)}{\overline{V}^2(s)} = \frac{K}{\tau s + 1} = \frac{\dfrac{1}{h(t)AR_{\text{coating}}}}{\dfrac{\rho cH}{h(t)}s + 1} \tag{2.7}$$

Where τ is the time constant and K is the gain. Time constant defines the period of time for the system to reach 63% of its steady state step response. Gain is a value which is proportional to the steady state step response of the system. With these two parameters the system dynamics can be completely described.

2.3 Theoretical Prediction for Internal Forced Convection HTC

A prediction of the heat transfer coefficient is prepared in order to specify the resistance across the coating, R_{coating}. In these experiments, the sample will be exposed to internal forced convection at an air temperature of 15 °C. Figure 2.2 shows the dimensions of the forced air apparatus. The sample will be located 1.57 m downstream of the axial blower, and the average velocity of the flow profile, V_{avg}, is 8.63 m/s.

For flow through non-circular tubes the Reynolds number, Nusselt number, and friction factor are based on the hydraulic diameter, D_{h}. In this work, only Reynolds number and Nusselt number are of interest.

$$D_{\text{h}} = \frac{4A_{\text{duct}}}{p} \tag{2.8}$$

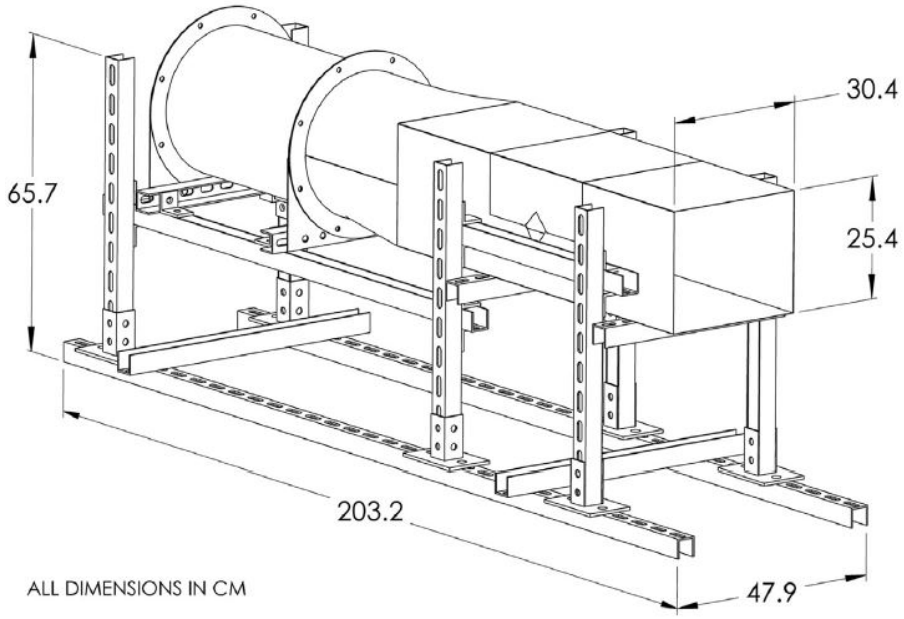

Figure 2.2: Duct Assembly used to provide Internal Forced Convection [44]

A_{duct} is cross sectional area and p is perimeter of the area. These parameters are calculated based on Figure 2.2.

$$D_{\text{h}} = \frac{4ab}{2(a+b)} = \frac{4 * 30.4[\text{cm}] * 25.4[\text{cm}]}{2 * (30.4[\text{cm}] + 25.4[\text{cm}])} = 27.68[\text{cm}] \tag{2.9}$$

2.3.1 Reynolds Number

Equation (2.10) describes how the Reynolds number is defined by its parameters: V_{avg}, D_{h}, and ν,

$$\text{Re}_{D_{\text{h}}} = \frac{V_{\text{avg}} D_{\text{h}}}{\nu} \tag{2.10}$$

Reynolds number is calculated for 3 scenarios and values for the Kinematic viscosity of air are sourced [45]. The scenarios represent the lowest possible, planned, and highest possible Reynolds numbers with this experimental setup. The film temperature, T_{f}, is typically used to evaluate properties of air. T_{f} represents the average of surface temperature, T_{sur}, and air temperature, T_{air}, Equation (2.11). In order to maintain conservative estimates, the sample temperature and air temperature will be treated as equivalent values for the minimum and planned cases. This is conservative because

in the minimum case, the sample will always be warmer than ambient air. For the maximum case, film temperature will be calculated for an air temperature of 25 °C and a sample temperature of 200 °C. This is maximum because air temperature will not increase significantly above room temperature (because there is no significant heat source present relative to the volume of air), and the sample cannot heat past 200 °C because the solder connections would melt.

$$T_f = \frac{T_{\text{air}} + T_{\text{sur}}}{2} \tag{2.11}$$

1. -30 °C Lowest possible film temperature.

2. 15 °C Air temperature planned for experiment.

3. 112.5 °C Highest achievable film temperature before failure of solder.

Film temperature -30 °C:

$$\text{Re}_{\text{D}_{\text{h1}}} = \frac{8.63[\text{m/s}] * 0.2768[\text{m}]}{1.087 * 10^{-5}[\text{m}^2/\text{s}]} = 219,759 \tag{2.12}$$

Film temperature 15 °C:

$$\text{Re}_{\text{D}_{\text{h2}}} = \frac{8.63[\text{m/s}] * 0.2768[\text{m}]}{1.470 * 10^{-5}[\text{m}^2/\text{s}]} = 162,502 \tag{2.13}$$

Film temperature 112.5 °C:

$$\text{Re}_{\text{D}_{\text{h3}}} = \frac{8.63[\text{m/s}] * 0.2768[\text{m}]}{2.360 * 10^{-5}[\text{m}^2/\text{s}]} = 101,220 \tag{2.14}$$

A higher Reynold's number indicates a more turbulent flow. Internal flow regimes are classified according to the ranges below. In the cases above, the flow regime will be turbulent if the blower is turned on.

$$\text{Laminar:} \quad \text{Re} < 2,300$$

$$\text{Transitional:} \quad 2,300 < \text{Re} < 10,000$$

$$\text{Turbulent:} \quad \text{Re} > 10,000$$

2.3.2 Entrance Region and Nusselt Number

The length of the channel for which the flow is developing defines the entrance region. Contact between the fluid inside the channel, and the internal walls of the duct result in the developing flow phenomena. As the boundary layer grows away from the internal walls of the channel, the flow profile across the cross section of the duct changes with axial length of the duct. The hydrodynamic length predicts the length of the duct for which the flow is developing. The same phenomena exists for thermal boundary layers, but in this case the duct and the fluid inside the duct are the same temperature, so no thermal boundary layer exists. According to [44] the entrance region for turbulent flows can be approximated with

$$L_{\mathrm{h,\,turbulent}} = 10D_{\mathrm{h}} = 10 * 27.7[\mathrm{cm}] = 2.77[\mathrm{m}] \tag{2.15}$$

The sample is located 1.57 m ($\frac{1.57}{0.277} = 5.7$ channel diameters) downstream from the blower; thus it is inside the entrance region. Figure 2.3 can be found on page 480 of [46], the following two observations are also found on page 480.

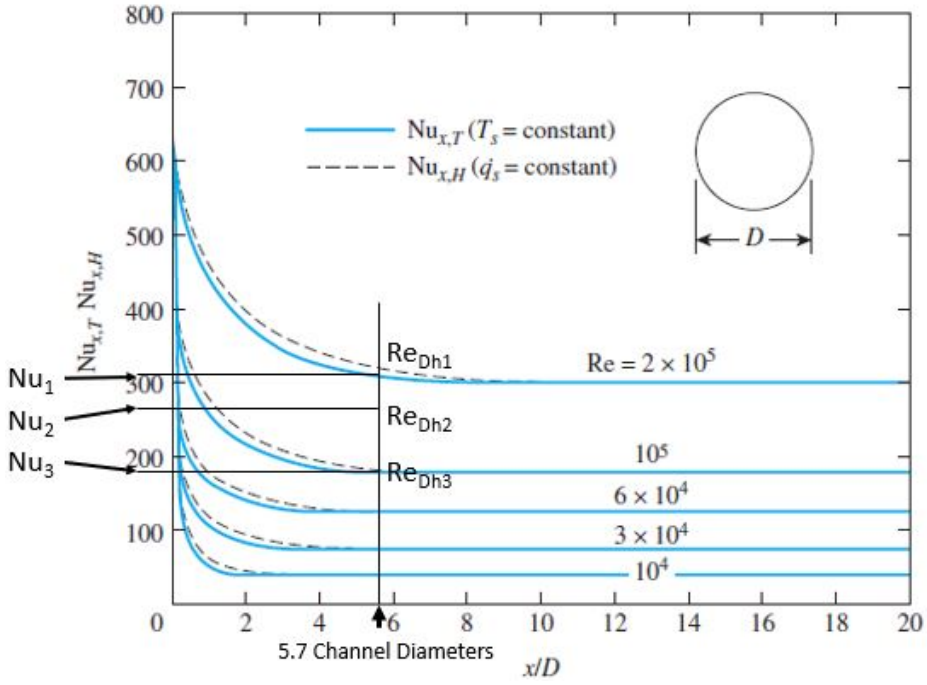

Figure 2.3: Reynold's Number to Nusselt Number Graphical Correlation [46]

- Nusselt number and thus HTC are higher in the entrance region
- If the Nusselt number is constant, then the flow can be assumed fully developed. Depending on Re, the Nusselt number may flatten out in a length shorter than $10D_{\mathrm{h}}$, and thus can be assumed fully developed.

For these experiments the Reynolds number is expected to range from $101,220$ to $219,759$ for 112.5 °C and -30 °C respectively. Using the graphical correlation in Figure 2.3 to determine respective Nusselt number values provides a means to estimate heat transfer coefficients.

For a film temperature of -30 °C the Reynolds Number inside the duct is $\mathrm{Re}_{\mathrm{D_{h1}}} = 219,759$, then a sample located 5.7 channel diameters downstream of the entrance will experience a Nusselt number of $\mathrm{Nu}_1 = 313$. For a Reynolds number of $\mathrm{Re}_{\mathrm{D_{h2}}} = 162,502$ the Nusselt number will be $\mathrm{Nu}_2 = 270$, and for a Reynolds number of $\mathrm{Re}_{\mathrm{D_{h3}}} = 101,220$ the Nusselt number will be $\mathrm{Nu}_3 = 185$.

2.3.3 Prediction of HTC

The forced convection heat transfer coefficient can be predicted using the correlation equation between Nusselt number and HTC.

$$h = \mathrm{Nu} \cdot \frac{k(T_f)}{l} \tag{2.16}$$

Where l is the length of the sample perpendicular to the flow of air and $k(T_{\mathrm{f}})$ [47] is thermal conductivity of air evaluated at the film temperature (Equation (2.11)). In this expression for HTC, the temperature of the steel block (T_{sur}) and environment (T_{air}) do not directly affect the prediction of the coefficient. These two parameters affect the film temperature, which in turn has an affect on HTC by changing the properties of air.

Table 2.1: HTC Prediction

Case	**Film Temperature** [°C]	**Re**	**Nu**	**k(T_f)** [W/mK]	**h** [W/m^{2}K]
1	-30	219,759	313	22.0	137.8
2	15	162,502	270	25.5	137.7
3	112.5	101,220	185	32.5	120.2

The last column of Table 2.1 depicts the prediction of HTC for each case. Across the film temperatures considered, HTC is expected to range by 14% with respect to the mean of the range. The HTC value of 138 W/m^{2}K will be used for the specification of resistance of the sample to be manufactured.

2.4 Thermal Dynamics Simulation for Sample Resistance Specification

According to Equation (2.7) R_{coating} is a parameter of gain but not a parameter of time constant. Increasing R_{coating} linearly would reduce gain of the temperature dynamics linearly. In order to specify an R_{coating} for manufacturing, minimum and a maximum steady state temperatures must be specified. Maximum and Minimum temperatures will be specified for the range of inputs: 3, 6, and 9 V. Maximum temperature will be specified from physical constraints of the system, and minimum temperature will be specified by expected levels of noise.

2.4.1 Gain Specification

Maximum Gain Specification

The solder used to make power connections to the sample melts at 200 °C. Thus, the sample's steady state temperature must be lower than 200 °C at 9 V.

Minimum Gain Specification

Figure 6a in [48] shows temperature curves created using the same cold room

to be used in this study. The environment air temperature is shown to fluctuate between -24 °C and -27.5 °C, with a period of 400 s (50 oscillations in 20,000 s), with a temperature set-point of -25 °C. Fluctuations in air temperature translate to fluctuations in temperature of the sample. Equation (2.5) is used to describe the relationship between air temperature and bulk material temperature. Voltage was set to zero and the equation was solved for $T(t)$.

$$T(t) = T_{\text{air}} + (T_{\text{i}} - T_{\text{air}}) * exp(-\frac{h}{\rho cH}t) \tag{2.17}$$

Thus if T_{air} fluctuates according to the sinusoidal equation below:

$$T_{\text{air}} = 15[^{\circ}\text{C}] + 1.75[^{\circ}\text{C}] * sin(\frac{2\pi}{400}t) \tag{2.18}$$

and $T_{\text{i}} = 15[^{\circ}\text{C}]$, then $T(t)$ will fluctuate as follows:

$$T(t) = 15[^{\circ}\text{C}] + 1.75[^{\circ}\text{C}] * sin(\frac{2\pi}{400}t) * (1 - exp(\frac{-h}{\rho cH}t)) \tag{2.19}$$

It is recognized in Equation (2.19), that the sample will see a temperature fluctuation nearly proportional to the fluctuation of air temperature. The gain shall be selected such that the temperature rise of the sample at steady state, is at least 3 times greater than the amplitude of the air temperature fluctuation. In this case, the steady state temperature must be at least 5.25 °C.

2.4.2 Resistance Specification Simulation

Taking the heat capacity and density of an AISI 1018 steel 2 cm thick sample to be 486 J/kgK and 7,870 kg/m^3 with a flame sprayed Joule heating element of area and resistance: 0.0069 m^2 and R_{coating}, and exposed to a HTC of 138 W/m^{2}K the voltage to temperature increase transfer function (Equation (2.7)) becomes:

$$\frac{\overline{\theta}(s)}{\overline{V}^2(s)} = \frac{K}{\tau s + 1} = \frac{\frac{1.05}{R_{\text{coating}}}[^{\circ}\text{C/V}^2]}{336[s] \cdot s + 1} \tag{2.20}$$

Voltage inputs of 3 V and 9 V were applied to Equation (2.20) in order to specify resistance for fabrication of the heating element. Low voltage inputs were used, because

providing higher voltages provides risk of electric shock. Working on systems of 30 V or higher requires certification [49]. The transfer function output is proportional to input voltage squared (V^2). Thus the range between the lowest and highest steady state temperature is minimized when input magnitudes are lower.

It is worth recognizing that gain reduces linearly with sample resistance increase, reducing the range between low and high steady state outputs, potentially permitting higher inputs depending on the application. The benefit which higher voltage inputs brings is reduced heat generation in sensor circuit components.

Table 2.2 shows predicted steady state values for a range of resistances at the inputs of interest. It is observed from this table that if R_{coating} is less than 1 Ω but greater than 0.5 Ω the steady state temperature from the planned inputs will meet the required specifications. Please see the code to generate these results in Appendix D.1.

Table 2.2: Steady State Temperatures (SST) at Resistances for Inputs of Interest

Coating Resistance [Ω]	SST: 3V Input [°C]	SST: 9V Input [°C]
0.25	37.8	340.2
0.5	18.9	170.1
1	9.5	85.1
2	4.7	42.5
3	3.2	28.4

2.5 Sensor Design for Resistance to Temperature Characterization

The objective of this sensor is to measure resistance of the sample with sufficient resolution in order to determine the $T(R)$ relationship of the Joule heating element. A multimeter did not suit this application because live measurements with time stamps

were required to be collected simultaneous to heating of the sample. A device with this capacity was not available. This requires that the sensor is able to produce a signal proportional to the resistance across the copper terminals of the sample while the sample is heating up. This relationship is important because the resistance across the joule heating element is one of two uncertain parameters in the transfer function (Equation (2.7)).

Section 2.4.2 specifies that the sample shall be manufactured with a resistance across the coating of $0.5\Omega < R_{\text{coating}} < 1\Omega$. This sensor was designed to measure variations around 2.3 Ω. Section 4.1 provides a discussion on why a sample of $R_{\text{coating}} = 2.3\ \Omega$ was utilized for the experimental portion of this study.

2.5.1 Circuit Design and Propagation of Error

In order to measure resistance across the coating, two measurements must be made: current through the coating and voltage drop across the terminals of the sample. Two voltage dividers in series were used to make these measurements. The first voltage divider measures voltage drop across a shunt resistor and the second voltage divider measures voltage drop across the sample, then these measurements are used to predict the resistance of the sample using Ohm's law. The specifications which guided the design of the sensor are listed below.

1. The sensor shall be able to measure resistance for all planned inputs while maintaining sufficient accuracy. Inputs are 3, 6, and 9 V and the sample will have a resistance of approximately 2.3 Ω, thus the sensor must be able to pass 3.9 A without melting.

2. This sensor shall continuously measure resistance to a relative uncertainty of 2 % or less. As observed in [38] the resistance of a sample coated with this material increased by 2 % after the connection to a power supply.

The first step in the design process is to address the accuracy specification. This is

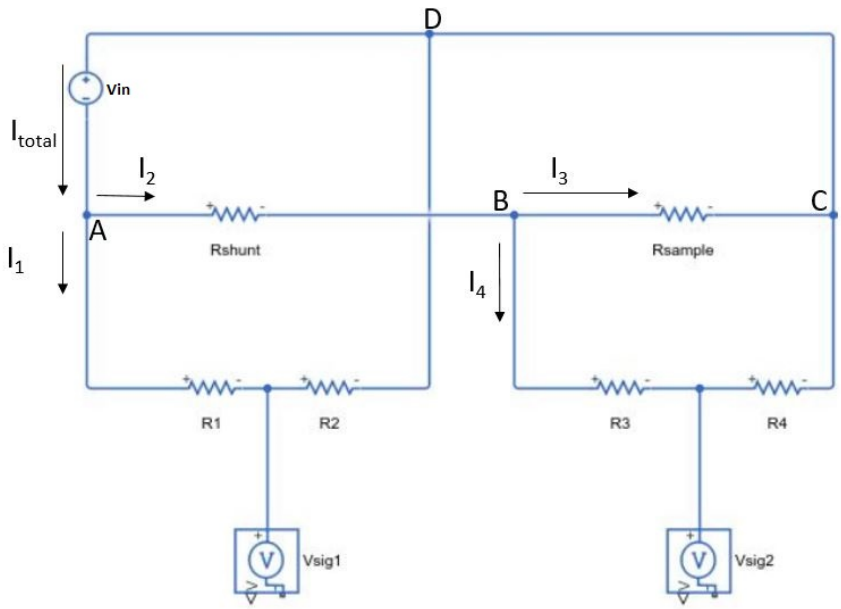

Figure 2.4: Circuit Layout for Double Voltage Divider Resistance Sensor

done using the voltage divider equations, and propagating error in order to determine the accuracy specifications for the hardware used to construct the sensor. Figure 2.4 describes the component layout for the resistance sensor. The signals received by the micro-controller (V_{sig1} and V_{sig2}) are described with the following equations.

$$V_{\text{sig1}} = V_{in} * R2/(R1 + R2) \tag{2.21}$$

$$V_{\text{sig2}} = (V_{in} - V_{shunt}) * R4/(R3 + R4 + R_{\text{shunt}}) \tag{2.22}$$

The voltages $V1$ and $V2$ are proportional to the voltage differences between nodes A and D and nodes B and C respectively. The following two equations describe the proportionality to the signal voltages.

$$V1 = V_A - V_D = V_{\text{sig1}} * (R1 + R2)/R2 \tag{2.23}$$

$$V2 = V_B - V_C = V_{\text{sig2}} * (R3 + R4)/R4 \tag{2.24}$$

The partial derivatives are determined for uncertainty propagation in order to specify the absolute uncertainty of the voltage measurements. This process is repeated for

$V2$. These two voltage measurements are used to predict properties of the sample.

$$\frac{\partial V1}{\partial V_{\text{sig1}}} = (R1 + R2)/R2 * dV_{\text{sig1}} \tag{2.25}$$

$$\frac{\partial V1}{\partial R1} = V_{\text{sig1}}/R1 * dR1 \tag{2.26}$$

$$\frac{\partial V1}{\partial R2} = V_{\text{sig1}}/R2 * dR2 - V_{\text{sig1}} * (R1 + R2)/R2^2 * dR2; \tag{2.27}$$

$$dV1 = \sqrt{\frac{\partial V1}{\partial V_{\text{sig1}}}^2 + \frac{\partial V1}{\partial R1}^2 + \frac{\partial V1}{\partial R2}^2} \tag{2.28}$$

Error propagation for current measurements. The purpose of the shunt resistor is to provide an estimation of current through the circuit.

$$I = (V1 - V2)/R_{\text{shunt}} \tag{2.29}$$

$$\frac{\partial I}{\partial V1} = dV1/R_{\text{shunt}} \tag{2.30}$$

$$\frac{\partial I}{\partial V2} = -dV2/R_{\text{shunt}} \tag{2.31}$$

$$\frac{\partial I}{\partial R_{\text{shunt}}} = -(V1 - V2)/R_{\text{shunt}}^2 * dR_{\text{shunt}} \tag{2.32}$$

$$dI = \sqrt{\frac{\partial I}{\partial V1}^2 + \frac{\partial I}{\partial V2}^2 + \frac{\partial I}{\partial R_{\text{shunt}}}^2} \tag{2.33}$$

Error propagation for Resistance measurements. The purpose of the second voltage divider is to predict voltage drop across the sample.

$$R_{\text{coating}} = V2/I \tag{2.34}$$

$$\frac{\partial R_{\text{coating}}}{\partial I} = -V2/I^2 * dI \tag{2.35}$$

$$\frac{\partial R_{\text{coating}}}{\partial V2} = dV2/I \tag{2.36}$$

$$dR_{\text{coating}} = \sqrt{\frac{\partial R_{\text{coating}}}{\partial I}^2 + \frac{\partial R_{\text{coating}}}{\partial V2}^2} \tag{2.37}$$

2.5.2 Hardware Specification

Equations (2.28, 2.33, 2.36) were used to specify required manufacturing tolerances in order to meet the sensor specifications described at the beginning of Section 2.5.1. Hardware was optimized for measuring a resistance value of 2.3 Ω with a maximum voltage input of 12 V. A voltage of 12 V delivered directly to a sample with a resistance of 2.3 Ω would draw 5.2 A. Though, because the shunt resistor (Figure 2.4) is in series with the Joule heating element, only 2.79 A would be delivered to the sample with a 12 V input to the sensor/heating-element circuit. Ideal component values are listed in Table 2.3, the performance of a sensor manufactured with these components is described in Table 2.4.

Table 2.3: Hardware Specifications for Resistance Sensor

Component	**Value** [Ω]	**Uncertainty** [±Ω]
$R1$	10,000	10
$R2$	2,000	2
$R3$	10,000	10
$R4$	2,000	2
R_{shunt}	2	0.02

Because $R1+R2$ is much greater than R_{shunt} and R_{sample}, I_{total} is taken to be equivalent to I_2. Thus, the measurement of current using the voltage drop across R_{shunt} is representative of the current through the whole circuit.

The measured values are predicted to be exposed to relative uncertainties of 1.042% for the I_{total} measurement and 1.050% for the R_{coating} measurement. These predic-

Table 2.4: Sensor Performance with Component Values Described in Table 2.3

Measured Property	**Value**	**Uncertainty**	**Unit**
I_{total}	2.792	$\pm$ 0.029	A
R_{coating}	2.298	$\pm$ 0.024	Ω

tions comply with the specifications listed in Section 2.5.1. Table 2.5 communicates predicted values for heat generation in each circuit component.

Table 2.5: Heat Generation in Circuit Components Described in Table 2.3

Component	**Generated Heat** [W]
$R1$	1.000e-10
$R2$	5.000e-10
$R3$	9.997e-11
$R4$	4.998e-10
R_{shunt}	15.597

Heat generated in the resistors $R1$, $R2$, $R3$, $R4$ are negligibly low because the current through these resistors is very low. High resistances were selected to ensure that current flows through the sample, instead of through the micro-controller. Current through the micro-controller is a concern for the following two reasons:

1. I_{total} would not be equivalent to I_2. This would impeded the measurement accuracy.

2. The micro-controller could be destroyed.

At a 12 V input over 15 W of heat is generated in R_{shunt}. It is necessary to specify a hardware component which is designed to manage this heat with a heat sink. Also,

the high amperage pathways of the Printed Circuit Board (PCB) were designed to a minimum trace width of 10 mm. The minimum trace width for a 1 oz/ft^2 copper board carrying 5 A is 7.19 mm. This calculation was made using the online trace width calculator [50].

Chapter 3

Experimental Method

Experiments were conducted to investigate the validity of the lumped capacity model, determine if the linear model can be used to approximate the non-linear behavior of the thermal system, characterize any uncertain parameters, and specify the effect of geometrical and material properties of the coating on the dynamics of the heating system.

3.1 Sample Fabrication

Using the flame spray process, a 138 cm^3 block of AISI 1018 steel was coated with a 69 cm^2 (approximately 40 μm thick) layer of NiCrAlY-Alumina 50 % by weight Metal Matrix Composite (MMC) as characterized in the study by Dehaghani *et al.* [38]. This coating material was selected for its high resistivity and weak relationship of temperature to resistivity [38]. Alumina was used as dielectic insulator between the conductive coating and the conductive steel sample [48]. Cold spray was applied to form copper terminals to create power connections [48].

3.1.1 Grit Blast

After the 2 cm thick steel sample was cut, grit blasting was used to increase surface roughness of the sample for greater adhesion of the flame sprayed alumina Layer. The sample was roughened with # 24 alumina grit (Manus Abrasive Systems Inc.,

Edmonton, AB, Canada) inside a dry blast unit (Model 48, Trinco, Fraser, Michigan, USA). The parameters describing the grit blast process are shown in Table 3.1.

Table 3.1: Grit Blast Parameters

Parameter and Unit	#24 Alumina Grit (Grit Blast)
Air Pressure [psig]	90
Air Temperature [°C]	25
Stand-off Distance [mm]	Approx. 40
Nozzle Horizontal Velocity [mm/s]	Approx. 10
Increment [mm]	Approx. 10
Passes [#]	1
Pre-heating Pass [#]	0

3.1.2 Flame Spray

A programmable robot arm (HP-20, Motoman, Yaskawa Electric Corp., Waukegan, IL, USA) was used to support and manipulate an Oxy-Acetylene flame spray torch (6PII, Oerlikon Metco, Westbury, NY, USA) while powder is fed to the torch nozzle using a volumetric powder feeder (5MPE, Sulzer Metco, Westbury, NY, USA) with Argon as the carrier gas. The parameters describing the flame spray deposition process for both coatings (insulating layer and joule heating layer) are shown in Table 3.2.

The thickness of the coating was estimated by measuring the thickness of the sample before and after any flame spray application using a manual micrometer (103-137, Mitutoyo, Takatsu, Kawasaki, Kanagawa, Japan).

Alumina

The spray parameters for Alumina (AMDRY 6060, Oerlikon Metco, Westbury, NY, USA) are based of the work done by Dehaghani et al. [38] and Rezvani Rad et al.

Table 3.2: Flame Spray Parameters

Parameter and Unit	Alumina (Flame Spray)	NiCrAlY-Alumina (Flame Spray)
Acetylene Flow [LPM]	22	20
Oxygen Flow [LPM]	32	30
Argon Flow [LPM]	9.3	9.3
Air Pressure [psig]	5	0
Air Temperature [°C]	25	N/A
Stand-off Distance [mm]	127	178
Nozzle Horizontal Velocity [mm/s]	300	500
Powder Feed [Flow Monitor Reading (FMR)]	100	40
Increment [mm]	3	4
Passes [#]	5	2
Pre-heating Pass [#]	1	0

[48]. A preheating pass prior to the application of the Alumina was performed in order to reduce the residual tensile stresses of the Alumina layer after coating [37]. Three thickness measurements were taken and averaged resulting in a mean thickness of 287 μm. An Alumina layer of 200 μm has shown to effectively insulate a joule heating layer constructed with flame spray [37].

NiCrAlY - Alumina 50%/50%

Alumina (AMDRY 6060, Oerlikon Metco, Westbury, NY, USA) and NiCrAlY (AMDRY 964, Oerlikon Metco, Westbury, NY, USA) were combined in equal parts, by weight, and mixed by agitation sealed inside a container. Thermal Spray Tape (170-10S Red, Green Belting Industries, Mississauga, ON, Canada) was applied to the edges of the sample to ensure no conductive particles formed pathways for electrons across the insulating Alumina layer (Figure 3.1b). Resulting from the uncertainty of the manufacturing process, it was necessary to iteratively construct a sample and change

spray parameters until a sample with desirable characteristics was obtained. When changing spray parameters linear relationships between feed rate, thickness, horizontal nozzle velocity and the output R_{coating} were assumed. The initial spray parameters for the MMC were derived from [38].

Resistance of the NiCrAlY-Alumina layer was measured at room temperature using a digital multimeter (34461A Dig. Multimeter, Keysight Tech., Mississauga, ON, Canada) in a Kelvin circuit after the cold sprayed copper tabs were applied.

3.1.3 Cold Spray

Table 3.3: Grit Blast, Flame Spray, and Cold Spray Parameters

Parameter and Unit	Copper (Cold Spray)
Air Pressure [psig]	92
Air Temperature [°C]	350
Stand-off Distance [mm]	5
Nozzle Horizontal Velocity [mm/s]	10
Powder Feed Rate [FMR or %]	5 %
Increment [mm]	N/A
Passes [#]	2
Pre-heating Pass [#]	0

Copper

A cold spray system (SST series P, CenterLine, Ltd., Windsor, ON, Canada) was used to apply Copper (Copper, SST-C5003, CenterLine, Windsor, ON, Canada) terminals to either end of the sample in order to make connections to a power supply. Using cold sprayed copper for this purpose was created in [48]. The spray parameters used in this process are described in Table 3.3. A Scanning Electron Microscope (SEM) image of the contact interface between the cold sprayed copper and flame spayed surface in

[37] shows that contact between the Copper and flame sprayed surface is very good. Figure 3.1c shows the finished product with cold sprayed copper terminals.

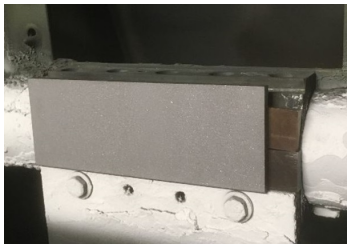

(a) Grit Blasted Steel Surface

(b) Alumina Surface with Spray Tape

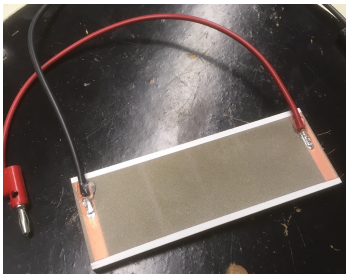

(c) NiCrAlY-Alumina with Copper Terminals

Figure 3.1: Sample Fabrication

3.2 Resistance Sensor Fabrication

Table 3.4 shows the model and source of resistors, micro-controller, and Copper PCB used to manufacture the Sensor. Resistance, maximum heat generation, and the manufacturing tolerance is shown for each resistor. This micro-controller supports 13-bit A/D conversion.

A PCB Computer Numerical Control (CNC) machine (Othermill Pro, Adafruit, New York, NY, USA) was used to cut the traces into the PCB. Eagle PCB design software (Eagle, AutoDesk, San Rafael, CA, USA) was used to generate the pathing specified to the CNC machine router head. See Figures B.1 and B.2 in Appendix B for Eagle software pathing layouts and component layouts for a preliminary prototype of the PCB. The early version of the PCB was built with too thin trace width to pass 5 A and the solder pads were too small to effectively make electrical connections. This was fixed for the final version of the PCB, see the final product in Figure 3.2.

Table 3.4: Sensor Materials

Item	Source
$R1$ & $R3$: 10 kΩ ±0.01 % 0.6 W	Foil Resistor, Vishay Intertech., Malvern, PA, USA
$R2$ & $R4$: 2 kΩ ±0.01 % 0.6 W	Foil Resistor, Vishay Intertech., Malvern, PA, USA
R_{shunt}: 1 kΩ ±1 % 100 W	Power Film , Riedon, Alhambra, CA, USA
Teensy 3.2	PJRC, Somerville, MA, USA
Printed Circuit Board (PCB)	FR-1 ,Bantam Tools, Peekskill, NY, USA

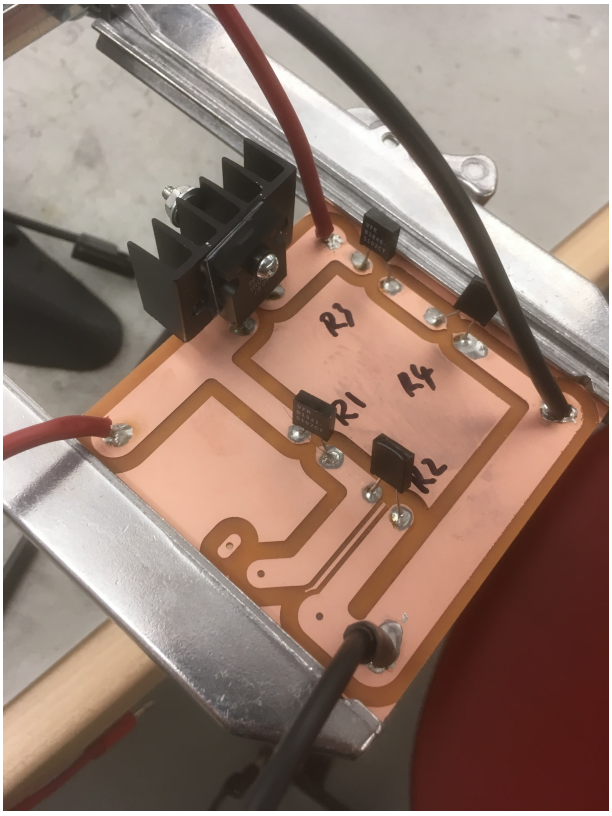

Figure 3.2: Manufactured PCB

3.3 Experimental Testing

3.3.1 Joule Heating Under Forced Convection Tests

Experiments were carried out in order to verify the capacity of Equation (2.7) to describe the temperature response of a joule heating element to a voltage input under forced convection conditions. A cold room (Foster Refrigerator USA, Kinderhook,

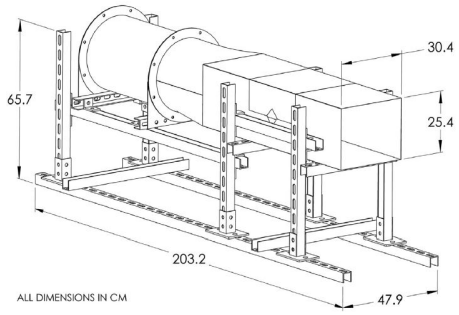

(a) Duct Assembly used to provide Internal Forced Convection [44]

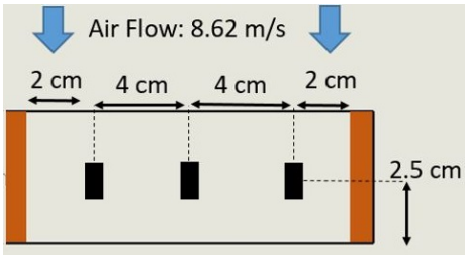

(b) Thermocouple Location and Air Velocity

Figure 3.3: Forced Air Apparatus and Sensor Orientation

NY, USA) was used to control air temperature to 15 °C. A power supply (1902B DC, B & K Precision Corporation, Yorba Linda, CA, USA) was connected to the leads of the sample (3.1c), in order to supply 3, 6, and 9 V inputs. A duct assembly inside the cold room (3.3a), houses a 0.25 kW blower (DDA-12-10033B, Leader Fan Industries, Toronto, ON, Canada) and was used to provide internal forced convection heat transfer conditions between the sample and air with an air velocity of 8.6 m/s. The air velocity was measured using a manometer [44].

Six thermocouples were used to collect temperature measurements from the sample. Three thermocouples on the surface, and three on the bottom between the sample and wood as depicted in Figure 3.3b. The surface measurements were averaged and compared to the average of the measurements taken from the bottom of the sample in order to confirm the application of the lumped capacity model. Leading and trailing edges are expected to have different heat transfer rates. Average heat transfer coefficient across the surface is used as a parameter in Equation (2.7), so temperature measurements were collected from the center of the sample. Assumption 1 in Section 2.1 describes that the edges of the sample are treated as insulated. Error is inevitable with this assumption: because some heat will be lost to convection at these edges. The heat loss will induce some temperature gradients along the edges of the sample. To not skew bulk temperature measurements, sensors were placed at the

center of the sample. As described in Section 2.2, coating materials with greater thermal conductivity can be selected to reduce inevitable temperature gradients across the surface.

Four measurement trials were carried out for each input condition, the condition of the K-type thermocouples (Omega, Montréal, QC, Canada) was reviewed after each set of trials and thermocouples were re-fixed if required. The thermocouples fed signals to a data acquisition system (SCXI-1600, National Instruments, Austin, TX, USA) and national instrument software (NI MAX, National Instruments, Austin, TX, USA) was used to interpret the data. Data was eliminated from analysis if it was produced with faulty thermocouples. The step input was held until the temperature response had reached a steady state, each experiment was run for 2,520 seconds. Time constant, gain, and heat transfer coefficient were extracted from the experimental data in order analyze and verify the first-order model described by Equation (2.7).

3.3.2 Resistance to Temperature Characterization Test

The $T(R)$ relationship was determined by measuring both resistance and temperature of the sample for as large a range as possible, given physical constraints. The hardware to supply power, create temperature measurements, and regulate air temperature were the same as for the experimental method described in Section 3.3.1.

The resistance sensor, design described in Section 2.5 and fabrication described in Section 3.2, was used to measure and interpret the signal proportional to resistance. The Teensy 3.2 (component of the sensor) sent the interpreted signal to a laptop during the experiment. The incoming data was formatted in a .txt file using the CoolTerm free software [51].

Power input and air temperature were varied from low to high conditions for the sample to cover as large a temperature range as possible, while remaining inside the operational specifications of the resistance sensor.

The cold room (Foster Refrigerator USA, Kinderhook, NY, USA) was initially set

to -25 °C. Over the course of the experiment, the set point was increased to 27 °C. Opening the door which separates the cold air, from warm building air, was used as a method increase the heating rate of air inside the cold room. The blower (DDA-12-10033B, Leader Fan Industries, Toronto, ON, Canada) inside the cold room was left on in order to elevate the HTC dictating heat transfer between the sample and the air. Voltage inputs ranged from 9 V to 12 V.

The following numbered list describes the power input and air temperature set point for each stage of this experiment. The parameters were changed to the next stage once the sample had reached a steady state temperature.

1. Input: 9 V and Air Set Point: -25 °C. Door closed.

2. Input: 12 V and Air Set Point: -25 °C. Door closed.

3. Input: 12 V and Air Set Point: 0 °C. Open door by 4° for 10 s period.

4. Input: 12 V and Air Set Point: 15 °C. Open door by 10° for 10 s period X 2.

5. Input: 12 V and Air Set Point: 27 °C. Open door by 90° for duration of stage.

The experiment was concluded once the sample temperature had reached steady state during the fifth stage.

Chapter 4

Results and Discussion

4.1 Experimental Resistance to Temperature Characterization Results

4.1.1 Actual Sample Resistance for Experiments

Section 2.4.2 describes the method to specify R_{coating} using theoretical predictions of parameters dictating the heating dynamics of the sample. It was later found that the HTC prediction used to make this specification was lower than that of the actual HTC which the sample is exposed to. The R_{coating} specified in this section is $(0.5\Omega < R_{\text{coating}} < 1\Omega)$. Despite this low theoretical HTC value, this specification would still produce samples which meet the requirements of this study.

During fabrication, difficulty was encountered in producing a sample which exhibited insulation between the conductive heating layer and the steel substrate. After trial and error, it was found that conductive particles from the Alumina-NiCrAlY spray process were forming a bridge across the Alumina insulating layer, thus eliminating the electrical insulation provided by the Alumina layer for current passing through the Joule heating element. In order to avoid this complication, thermal spray tape was used to cover the edges of the sample prior to this step in the fabrication process, see Figure 3.1b in Section 3.1. This effectively eliminated the problem. Finally, a sample of 2.3 Ω with thickness of 40.6 μm was produced which exhibited insulation between the joule heating layer and the substrate. Despite the R_{coating} not

residing inside the specification, this sample was used for this study since the heating dynamics it exhibited were suitable for the conditions in this study.

4.1.2 Resistance to Temperature Characterization

Figure 4.1 shows the raw temperature data and the raw resistance signal correlating to the increasing temperature of the sample. The numbers 1 through 5 in 4.1a indicate the stages of the experiment as described in Section 3.3.2. Cold room set point, the degree of which the cold room door was opened, period of opening the door, and the number of times the door was opened are variables.

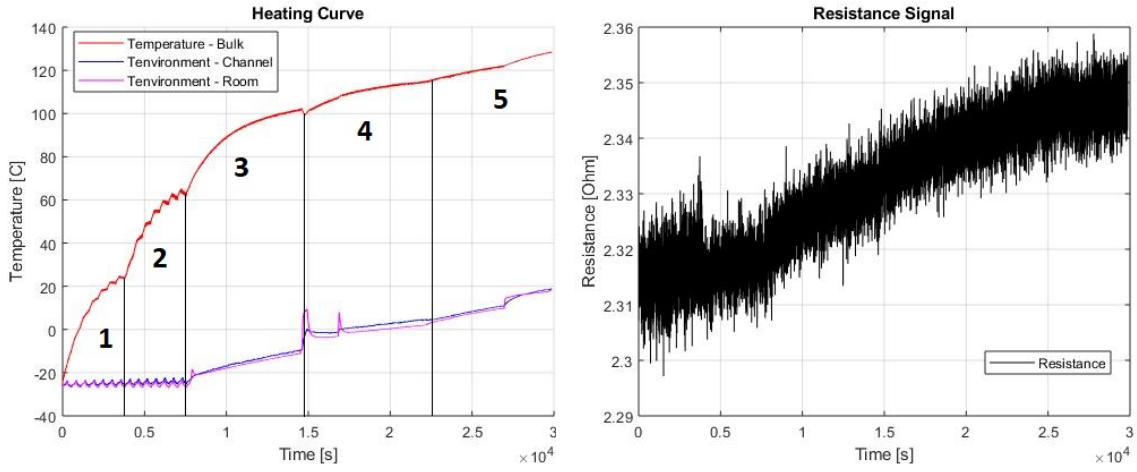

(a) Temperature (b) Resistance

Figure 4.1: Raw Data

Observation of the raw resistance signal in 4.1b confirms the necessity of digitally filtering the data in order to accurately determine the relationship of temperature to resistance. Figure 4.2 shows the raw resistance data compared against two filtered data sets. One data set is produced with a 10 point moving average and the other data set is produced with a 100 point moving average. Zero phase filtering was applied by using the `filtfilt` function in MATLAB® . This function convolutes the data set in one direction (forward), then convolutes the data set in the other direction (backward), effectively eliminating the phase difference between the filtered and unfiltered data sets. Also, the function mirrors the length of data equivalent to

filter window width along the x-axis and y-axis at the endpoints. This removes the end effects of the moving average filter. A drawback of this filtering technique is that it cannot be used in live systems, it can only eliminate the phase difference resulting from filtering in static data sets. The leading and trailing filter width data points were trimmed from the filtered data set, despite the mirroring aspect of this function. The 100 point moving average was used for further analysis in this work. Equation (4.1) is the transfer function describing the relationship between the z transform of the input and the z transform of the output for the 100th order Finite Impulse Response (FIR) filter.

$$\frac{Y(z)}{X(z)} = \frac{\frac{1}{100} + \frac{1}{100}z^{-1} + ... + \frac{1}{100}z^{-100}}{1} \tag{4.1}$$

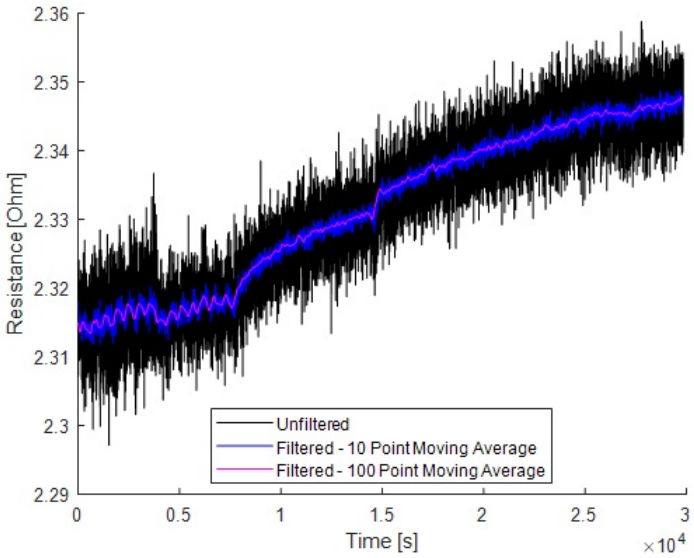

Figure 4.2: Filtered Resistance Data

The filtered data set is plotted against the temperature curve in Figure 4.3. Finally, the temperature to resistance correlation for the Alumina-NiCrAlY coating was determined by plotting resistance versus temperature and fitting the data set with a 3rd order polynomial in Figure 4.4.

Equation (4.2) describes the line used to fit the resistance to temperature correlation for the 40.6 μm thick Alumina-NiCrAlY 50 %/50 % coating which is 5 cm wide

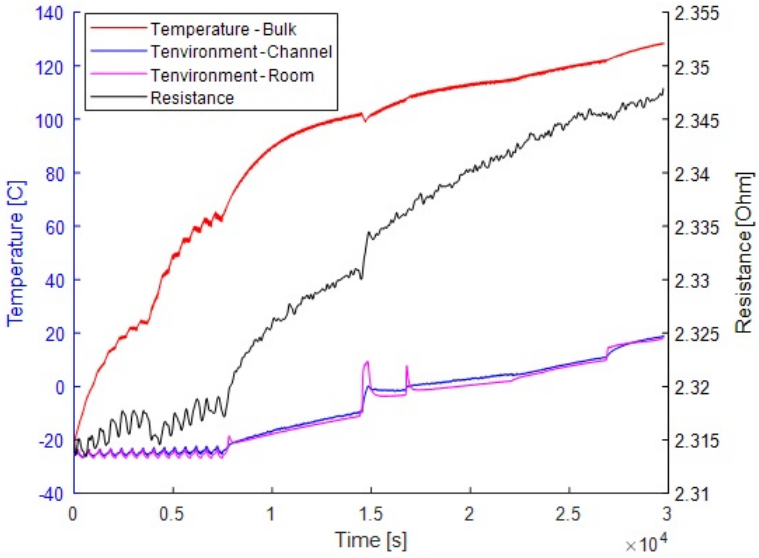

Figure 4.3: Temperature Experimental Data

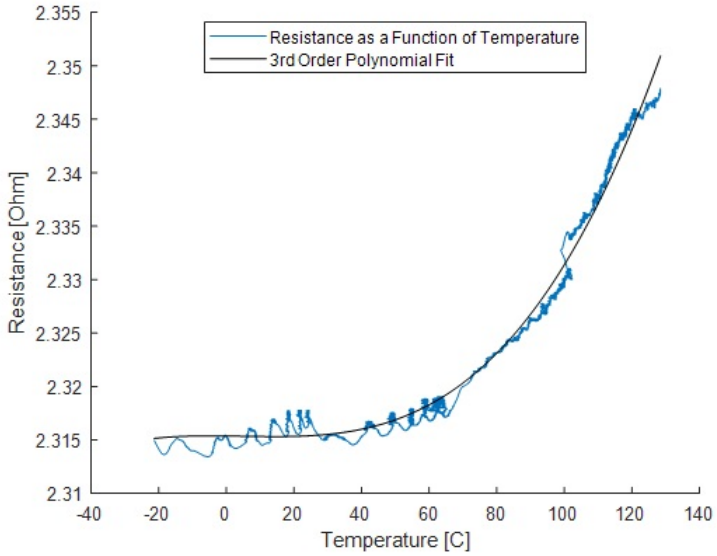

Figure 4.4: Filtered Resistance Experimental Data

and 12 cm long.

$$R(T) = 1.91 * 10^{-8} \left[\frac{\Omega}{^{\circ}\mathrm{C}^3}\right] \cdot T^3 - 2.69 * 10^{-7} \left[\frac{\Omega}{^{\circ}\mathrm{C}^2}\right] \cdot T^2 - 3.99 * 10^{-6} \left[\frac{\Omega}{^{\circ}\mathrm{C}}\right] \cdot T + 2.32\ \Omega \tag{4.2}$$

$$R_{\text{coating}} = \varrho \frac{D}{A_{\text{coating}}} \tag{4.3}$$

Equation (4.3) is used to generalize Equation (4.2) into Equation (4.4) to describe

resistivity of the Alumina-NiCrAlY 50 %/50 % material, instead of the resistance of the coating on this sample.

$$\varrho(T) = 3.23{*}10^{-7}\left[\frac{\mu\mathrm{m}\Omega}{^{\circ}\mathrm{C}^3}\right]\cdot T^3 - 4.55{*}10^{-6}\left[\frac{\mu\mathrm{m}\Omega}{^{\circ}\mathrm{C}^2}\right]\cdot T^2 - 6.74{*}10^{-5}\left[\frac{\mu\mathrm{m}\Omega}{^{\circ}\mathrm{C}}\right]\cdot T + 39.2\ \mu\mathrm{m}\Omega \tag{4.4}$$

Figure 4.4 shows that the resistance of the coating had increased by 1.5% between the temperatures of -20 °C and 130 °C. Unfortunately, these results are derived from only one experimental trial. This is a result of the University shutdown at the time of the creation of this thesis. In order to ensure accuracy of this one trial, the performance of this sensor is evaluated in Figure B.3 of Appendix B. Any conclusions from the numerical evidence in this section would require checking with further experimental studies.

Literature indicates the resistivity of this coating material to be 93.5 $\Omega\mu$m [38] measured at room temperature (assume 25 °C). [38] also indicates that the resistance of the sample from which this resistivity was derived only changed by 2% after connection to the power supply. At 25 °C, Equation (4.4) predicts a resistivity of 39.2 $\Omega\mu$m. This is a 82% deviation with respect to the mean of the two resistivity values. This deviation is a result of a number of factors:

1. Differing porosity and particle oxidation of the coatings. The spray parameters in this study were derived, and changed, from the paramaters which were used to produce the sample in [38].

2. Different thickness measurement techniques. In this study, thickness was measured using a manual micrometer whereas in [38] thickness was measured using an SEM.

3. Single trial used to create results for this study. [38] indicates that the reported resistance values were produced as an average from a number of samples.

Figure 4.4 shows that resistance changed negligibly over the temperature range of this

experiment (-40 °C and to 5 °C). Depending on the application of the Joule heating element, this negligible change can either be desirable or a problem. For example, if temperature predictions are created from resistance measurements, it would be beneficial to use a coating material which exhibits a stronger relationship between temperature and resistance. On the other hand, if a transfer function is being used for model-predictive-control, it would be beneficial if the coating resistance has a negligible correlation to temperature. In order for the results in this section to be used in any application, it would be required to collect more data.

4.2 First-order Linear Model Temperature Dynamics

Alumina has the interesting property of effectively insulating electricity while providing a conductive pathway for heat. In this study, this is beneficial because with the lumped capacity model, the steel block and the coating are treated as a single entity with no thermal contact resistance. This assumption is valid because of the high thermal conductivity of Alumina, and high contact area between at each coating interface.

The MMC used for Joule heating was selected for its high resistivity and weak dependence on temperature when compared to other coating materials [38]. According to Equation (2.7), a linear increase in resistance across the power terminals of the sample (R_{coating}) results in a linear decrease of steady state temperature. Resistance across the power terminals is entirely determined by the properties of the thermal coating used to construct the joule heating element.

12 trials were performed for this study; unfortunately, 7 trials were eliminated because the temperature sensors used to collect the data produced unreliable readings. It was not possible to obtain more experimental data because of the university shutdown. Standard deviations are used here to show the similarity between multiple trials used to generate the data, due to the small sample size, they do not represent

a normal distribution.

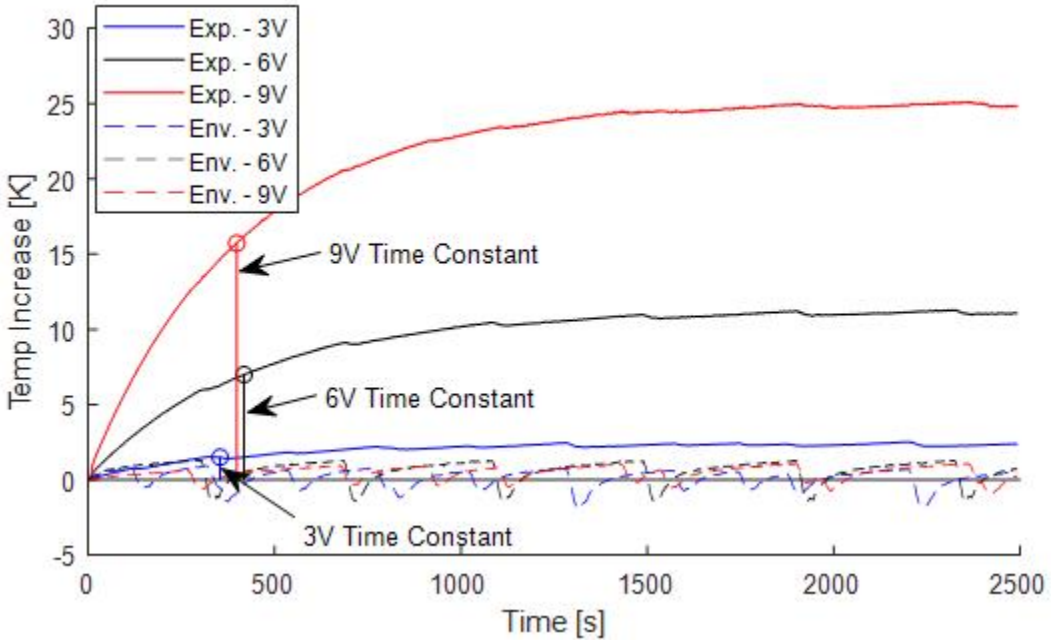

Figure 4.5: Sample Heating Temperature Dynamics

The sample drew 3.9, 15.6, and 35.1 W over the duration of the experiment for each input voltage 3, 6 and 9 V, respectively. Therefore, the resistance of the sample changed negligibly over the tested temperature, this agrees with the work shown in Section 4.1. See Figure 4.5 for the temperature dynamics of the heating system created with the NiCrAlY-Alumina MMC. The dotted lines show environment air temperature, fluctuations are a result from the compressor cooling unit turning on and off in order to maintain the 15 °C setpoint. The curved lines represent bulk temperature of the steel sample normalized to the initial environmental temperature. Steady state temperature increases were measured to be 2.38, 11.06, and 24.88 °C with standard deviations (n=2,1,2) of 0.59, 0, and 0.21 °C for each respective input. From the steady state temperature increases, gain was determined to be 0.265, 0.307, and 0.307 $C°/V^2$ with standard deviations (n=2,1,2) of 0.066, 0, 0.003 $C°/V^2$. With respect to the mean, gain varies by 15 % given the heat transfer conditions and voltage inputs. For the given inputs, time constant was determined to be 354, 418, and 399

s, varying by 17 % with respect to mean, and with standard deviations (n=2,1,2) of 2.5, 0, and 5.0 s. The 15 % and 17 % variations in gain and time constant show that the first-order linear model approximation is valid to estimate the dynamic response of the thermal system to the input voltage to the power of two.

4.3 Experimental Determination of HTC

Equation (2.5) can be re arranged to solve for HTC:

$$h(t) = \frac{V^2/R_{\text{coating}} - \rho cAH\frac{dT}{dt}}{A * (T(t) - T_{\text{inf}})} \tag{4.5}$$

Applying a finite difference to the derivative:

$$\frac{dT}{dt} = \lim_{d\to 0} \frac{T(m+d) - T(m)}{d} \tag{4.6}$$

Results in a discrete expression for HTC:

$$h(m) = \frac{1}{A * (T(m) - T_{\text{inf}}(m))} \cdot \left[V^2/R_{\text{coating}} - \rho cAH * \frac{T(m+d) - T(m)}{d}\right] \tag{4.7}$$

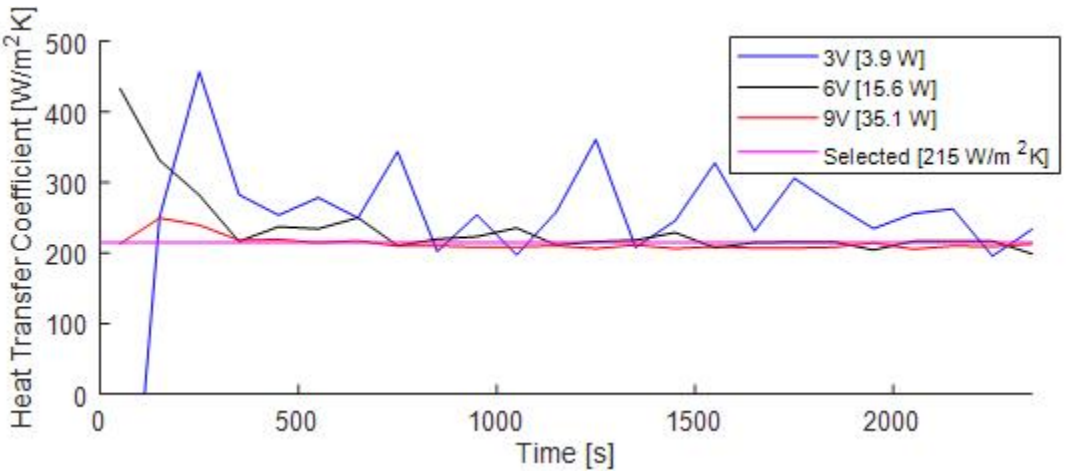

Figure 4.6: Heat Transfer Coefficient Characterization

Equation (4.7) was used to predict the HTC from experimental data. Figure 4.6 shows the resulting HTC predictions for each input voltage. Prior to 150 s the predictions are unnatural. This is a result of transient behaviors that change for each

trial. For example, for an input of 3 V, the measured HTC was initially negative because the air temperature is initially greater than the sample temperature, and it showed large fluctuations, as a result of the large relative disturbance produced by the compressor unit. The measured HTC for inputs of 6 V and 9 V were more stable and were between 208 W/m^{2}K and 250 W/m^{2}K. Section 2.3 describes the theoretical prediction of the heat transfer coefficient for this scenario to be 138 W/m^{2}K. This value was used to make an initial specification for R_{coating}, the implications of this were discussed in Section 4.1.1. The predicted value varies from the experimental values by 40 % and 58 %. For the purposes of verifying Equation (2.7) and checking the Biot number, an HTC value of 215 W/m^{2}K was chosen to represent the heating conditions based on the experimental results.

4.4 Biot Assumption

Table 4.1 shows the steady state temperature increases measured by the thermocouples located on the coating's surface (n=3), the thermocouples located on the sample's bottom (n=3), and the difference between these values. 3.1, 3.0, and 3.9 % of difference between the coating's surface and the sample's bottom was observed for an input voltage of 3, 6 and 9 V, respectively for the 2 cm thick sample. This confirms the validity of using the Biot assumption under these heating conditions and sample dimensions. The Biot number for this scenario is 0.08, which is only slightly less than 0.1, though the difference between the surface and bottom temperatures is small enough for the assumption to be valid and useful. With a greater value for HTC and a more thick sample than what was tested, this assumption becomes increasingly less accurate. For the application of this model, it is important to check that the Biot number is less than 0.1 to ensure accuracy.

Table 4.1: Steady State Temperatures

	SST: Surface [°C]	SST: Bottom [°C]	SST: Bottom - Surface [°C]
Trial 2: 3V	1.99	1.93	-0.06
Trial 3: 3V	2.76	2.84	0.09
Trial 5: 6V	10.82	11.31	0.49
Trial 6: 6V	11.86	12.03	0.18
Trial 8: 9V	24.46	25.59	1.13
Trial 9: 9V	24.32	25.14	0.83

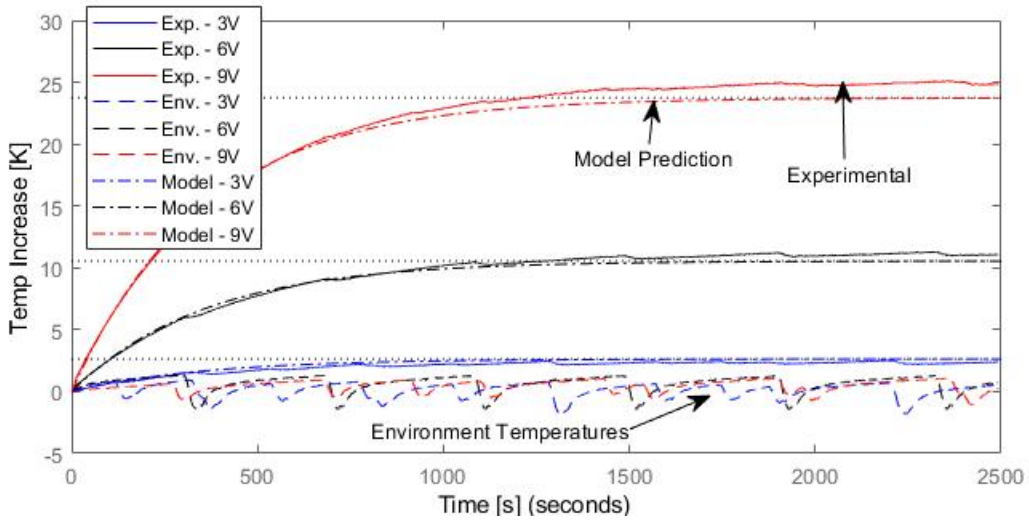

Figure 4.7: Transfer Function (Equation (2.7)) V.S Experimental Data

4.5 Transfer Function Verification

Taking the heat capacity, density, and thermal conductivity of an AISI 1018 steel, 2 cm thick sample to be 486 J/kgK, 7,870 kg/m^3, and 51.9 W/mK with a flame sprayed resistive heating element of area and resistance: 0.0069 m^2 and 2.3 Ω, and exposed to a HTC of 215 W/m^{2}K (selected) the transfer function, Equation (2.7), becomes:

$$P(s) = \frac{\overline{\theta}(s)}{\overline{V}^2(s)} = \frac{K}{\tau s + 1} = \frac{0.32[\frac{^\circ C}{V^2}]}{336[s] \cdot s + 1} \tag{4.8}$$

This equation describes the dynamic behavior of the thermal system in response to a step-like increase in voltage. Using Equation (4.8), step responses of the thermal system to input voltages 3, 6, and 9 V were simulated and plotted against the collected experimental data in Figure 4.7. Also, Figure 4.6 shows how the selected HTC compares to the experimentally measured HTC values. For 3, 6, and 9 V inputs, the steady state temperature increases predicted by the model are 2.9, 11.5, and 25.9 °C and the experimentally determined steady state temperature increases are 2.4, 11.1, and 24.9 °C, indicating 18.9, 3.5, and 3.9 % of differences. For each input, the time constants measured were 354, 418, and 399 s while the time constant predicted by the model is 336 s, correlating to 5.2, 21.8, and 17.0 % differences.

The percent differences shown above are largely a result from the fluctuating air temperature inside the cold room in combination with the low number of trials used to create the data. The final temperature of the sample largely depends on at what point is the cold room in its warming and cooling cycle. The cold room air temperature fluctuates with a range of 3.8 °C when set to 15 °C. More trials would mitigate this affect.

Equation (4.8) describes a linear time-invariant dynamical system used to model a non-linear process. The parameters ρ, c, A, and H change negligibly with the operation of the joule heating element. In this study, R_{coating} changed very little (maximum 2%) with the operation of the element, this depends on the material used to construct the coating. In application of Equation (2.7), HTC changes non-linearly with respect to a number of factors: air velocity, air temperature, air moisture, and thickness of ice accretion.

This work shows a method to determine HTC from the operation of the heating element using only temperature sensors. If more accuracy from the model is required: the HTC value can be predicted with a non-linear model or the sensor derived HTC value can be used as an input to the linear model. These are alternatives available to assuming a constant HTC parameter. If surface temperature measurements are

available in operation, the HTC value can be predicted using a discrete numerical equation similar to Equation (4.7).

4.6 Transfer Function Sensitivity Study

The work in this section evaluates the sensitivity of the first order model to the parameters that describe it. Resistance across the terminals (R_{coating}) and HTC are the uncertain parameters which will be examined in this study. ρ, c, A, H are the other parameters in Equation (2.7), but they vary negligibly with the operation of the heating element.

The sensitivity of the transfer function to these parameters is examined independently, then the combined affect of their uncertainties is examined. The transfer function was verified using data generated with an ambient air temperature of 15 °C and exposed to internal forced convection at an airspeed of 8.6 m/s. The maximum and minimum ranges of the uncertain parameters are defined from experimental data shown in Section 4.1 and Section 4.3. The certain values and nominal uncertain values for the AISI 1018 steel sample and the heat transfer conditions it is under are listed below.

- $\rho = 7870$ kg/m^3
- $c = 486$ J/kgK
- $A = 0.0069$ m^2
- $H = 2$ cm
- $h_{\text{nominal}} = 215$ W/m^{2}K
- $R_{\text{nominal}} = 2.3\ \Omega$

4.6.1 Sensitivity to Resistance

Resistance was taken to vary by ±2%, based on the discussion in section Section 4.1. A relative uncertainty of 1.05 % is added to account for a measuring device, resulting in a combined uncertainty of ±2.3%. The 9 V step response is calculated for 22 cases where the resistance value is sampled randomly within the uncertainty range defined for 20 cases, the remaining 2 cases represent the limit of the uncertainty range. Responses shown in figure 4.8. Maximum steady state temperature of 24.3 °C occurs at minimum resistance (2.25 Ω). Minimum steady state temperature of 23.2 °C occurs at maximum resistance (2.35 Ω).

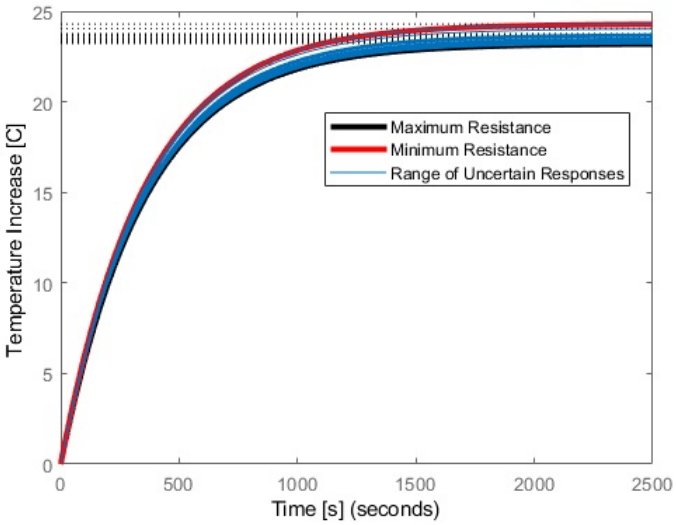

Figure 4.8: R Sensitivity

4.6.2 Sensitivity to HTC

The measurement of HTC was taken to be uncertain within the range of 208 W/m^{2}K and 250 W/m^{2}K. These limit values were selected based on the HTC measurements shown in Section 4.3, they represent the largest and smallest measured values for HTC. The 9 V step response is calculated for 22 cases where the value h is sampled randomly within the uncertainty range defined, and two cases represent the limits. Responses shown in figure 4.9. Maximum steady state temperature of 24.5 °C occurs

at minimum HTC (208 W/m^{2}K). Minimum steady state temperature of 20.4 °C occurs at maximum HTC (250 W/m^{2}K).

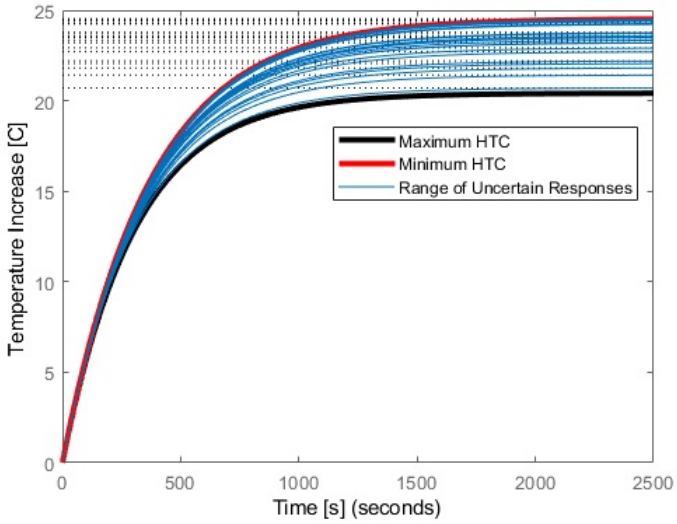

Figure 4.9: HTC Sensitivity

4.6.3 Sensitivity to HTC and Resistance

Here, the combined affect of the uncertainty values are evaluated. R limits are defined in Section 4.6.1 and HTC limits are defined in Section 4.6.2. The 9 V step response is calculated for 20 cases where the value h and R are sampled randomly within the uncertainty ranges, and two cases represent limits. Responses are shown in figure 4.10. Maximum steady state temperature of 25.1 °C occurs at minimum HTC (208 W/m^{2}K) and minimum resistance (2.25 Ω). Minimum steady state temperature of 20.0 °C occurs at maximum HTC (250 W/m^{2}K) and maximum resistance (2.35 Ω).

The range of steady state temperature values resulting from the combined uncertainties is 5.1 °C located at a minimum temperature of 20.0 °C, the range is 26 % of the minimum value. The 5.1 °C steady state temperature range results from an uncertain HTC range of 42 W/m^{2}K located at a minimum of 208 W/m^{2}K (20 %) and a resistance range of 0.1 Ω located at a minimum of 2.25 Ω (4.4 %).

Transfer function was shown to effectively predict the dynamics of the system in Section 4.5. According to the work in this section, the key to successfully applying this

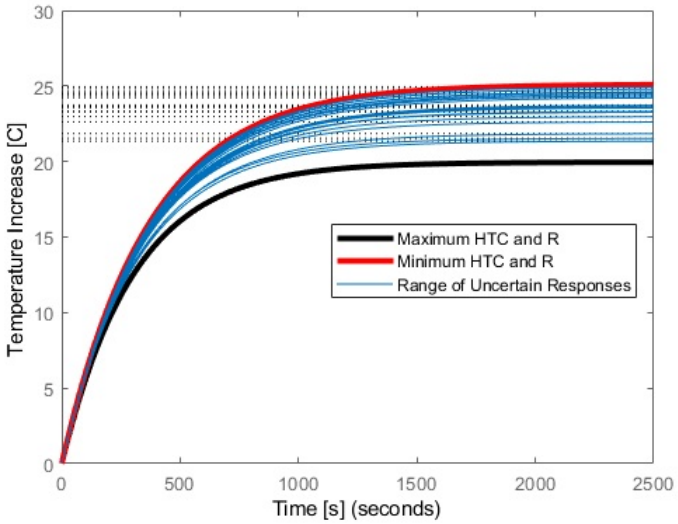

Figure 4.10: R and HTC Sensitivity

model to predict temperature dynamics of a heating system, it to refine the estimate of HTC used in the definition of time constant and gain. Equation (4.7) applies the simplest method available (forward finite difference) in order to estimate the temperature derivative with respect to time. This could be improved in a number of ways:

- Applying a higher order numerical discretization. For a live system a backward difference must be applied.
- A low pass temperature signal to make the HTC prediction. This would reduce volatility of the HTC prediction but would also introduce some phase lag.
- A Kalman filter to combine sensor reading from the discrete HTC prediction and theoretical predictions from a regression model. This could reduce noise and result in a higher confidence prediction than either approach independently.

4.7 Control System Design and Simulation

Section 4.5 and Section 4.6 justify that the transfer function, Equation (2.7), can be used to usefully predict the dynamics of the heating system described in Section 2.1.

The transfer function was used to simulate a system including a controller. The simulation was used to tune the gains of the controller. Gains were selected to optimize for set point tacking speed without exhibiting overshoot or steady state tracking error. Equation (4.9) describes the transfer function of a PID controller in the s domain. A PI controller is a PID controller with $K_\mathrm{d} = 0$.

$$C(s) = K_\mathrm{p} + \frac{K_\mathrm{i}}{s} + K_\mathrm{d}s \tag{4.9}$$

Proportional gain suggests an control input proportional to the difference between the set-point and the plant state. Integral gain suggests a control input proportional to the sum over time of the difference between the set-point and plant state, and is useful to eliminate steady state tracking error. Derivative gain suggests a control input proportional to the rate of change of the set-point and plant state, and is useful to respond to rapid disturbances in the state of the plant. Here, the plant state is temperature. A PI controller is used, instead of a PID controller, so filtering of the error signal is not necessary. High frequency noise results in rapid changes of the error signal. Without filtering this results in a volatile control output. If proportional gain is too high, overshoot, and potentially oscillation, will occur. If integral is too high, oscillation can occur. If integral gain is too low, set point tracking can be slow, or steady state tracking error is present.

Equation (4.8) was used in the simulation of the controller. In the s domain, convolution is operated as multiplication in the time domain. Performing $C(s) * P(s)$ (with $K_\mathrm{d} = 0$) results in the open loop transfer function 4.10.

$$G(s) = C(s) * P(s) = \frac{K_\mathrm{p}Ks + K_\mathrm{i}K}{\tau s^2 + s} = \frac{0.32K_\mathrm{p}s + 0.32K_\mathrm{i}}{336s^2 + s} \tag{4.10}$$

Where the closed loop transfer function is described below.

$$H(s) = \frac{G(s)}{1 + G(s)} = \frac{K_\mathrm{p}Ks + K_\mathrm{i}K}{\tau s^2 + (1 + K_\mathrm{p}K)s + K_\mathrm{i}K} = \frac{0.32K_\mathrm{p}s + 0.32K_\mathrm{i}}{336s^2 + (1 + 0.32K_\mathrm{p})s + 0.32K_\mathrm{i}} \tag{4.11}$$

Equation (4.11) describes a non-standard second order transfer function. As a result the standard relationships for rise time, overshoot, peak time, and settling time do not apply. Understanding of these performance specifications can be used as a guideline during the tuning process. For example, if overshoot is too high, then damping should be increased. If rise time is too slow, natural frequency should be increased. If transient behavior persists for too long, the poles need to be moved further left in the s-plane [52].

By adding a PI controller and feedback loop, a pole and a zero were added to Equation (4.8). The zero has a location of $s = -\frac{K_\mathrm{i}}{K_\mathrm{p}}$ in the s-plane. The poles are located at $s_{1,\,2} = \frac{-(1+0.32K_\mathrm{p})\pm\sqrt{0.10K_\mathrm{p}^2+0.64K_\mathrm{p}-430K_\mathrm{i}+1}}{672}$. The locations of the poles and zero in the s-plane change as proportional and integral gains change, this occurs during the tuning process. The system remains stable as long as the real component of the poles remains negative. If the poles have an imaginary component, the output will exibit oscillation. As long as the statement in Equation (4.12) is maintained, the system output remains non-oscillatory.

$$430K_\mathrm{i} < 0.01K_\mathrm{p}^2 + 0.64K_\mathrm{p} + 1 \tag{4.12}$$

Simulink was used to tune the gains for a 5 °C temperature increase. For instructions of how to use the tuner interface, and a screen shot of the interface, please see Appendix C. Gains are listed below.

$$K_\mathrm{p} = 32.027 \tag{4.13}$$

$$K_\mathrm{i} = 0.0955 \tag{4.14}$$

4.7.1 Control System Performance

The typical operating range for thermoelectric deicing elements is -5 °C to -40 °C. Simulations for the required voltage input, power draw, and energy delivery were plotted for the temperature increase set points of 5, 20, and 40 °C. Also, simulations examining disturbance rejection capability of the control system were performed.

Temperature Response, Voltage Input, and Windup Control

Figure 4.11 shows that overshoot is occurring for the 20 °C and 40 °C set point simulations. This overshoot is a result of integrator windup. While the set point is less than the state of the plant, the integrator term will instruct the power supply to send an increasingly large input to the heating element. If the power supply is sending the maximum input to the system, integrator windup occurs. The state of the plant must increase above the set point in order to subtract away the excess integrator error. Integrator error occurs for all of the simulations shown, but it is more pronounced the longer the power supply is saturated at 12 V, see Figure 4.12. A second simulation included wind up control in the PI controller. Results are shown in Figures (4.11, 4.12, 4.15, 4.16) with the solid lines.

These results were generated using the Simulink block diagram shown in Figure C.1, then the data was exported to MATLAB® and plotted with the code shown in D.4.

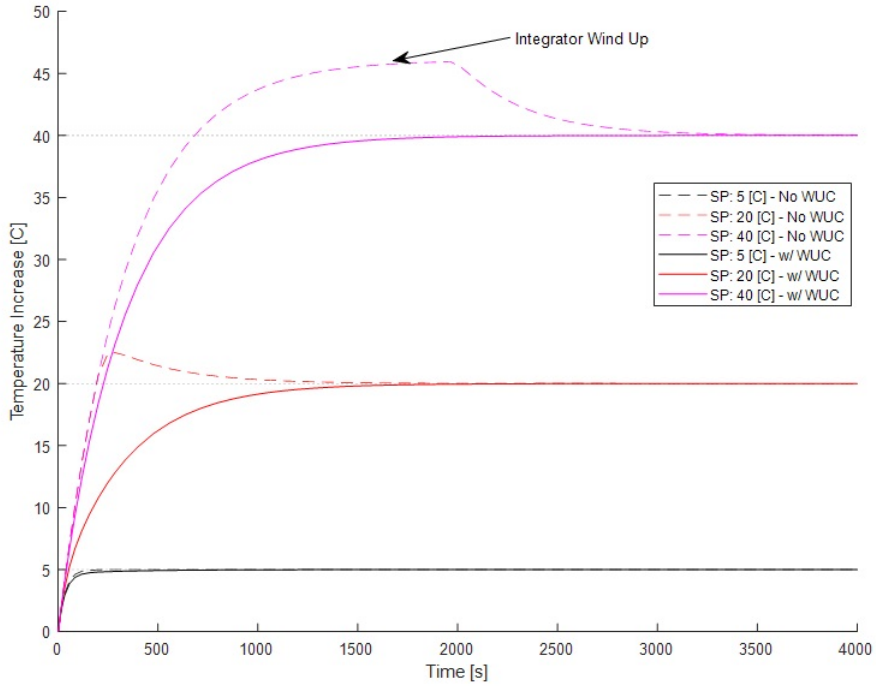

Figure 4.11: Temperature Increase Output as a Function of Time

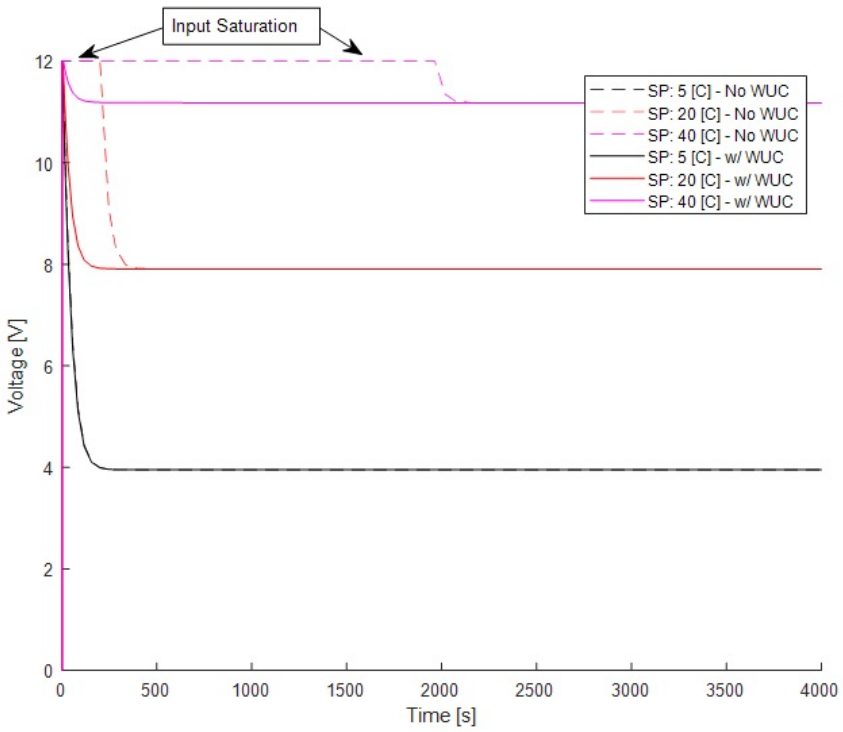

Figure 4.12: Voltage Input

Disturbance Rejection

A step disturbance of -10 °C was applied at 2000 s for simulations examining 5, 20, and 40 °C temperature set point increases. This simulates a rapid drop in temperature of the sample, and how the system would respond to such a drop. Figure 4.13 shows that for 5 and 20 °C set points, the disturbance is corrected in 500 s and 1500 s respectively. Though, for the 40 °C set point simulation, a steady state error of 4 °C exists after the disturbance. The reason for this is understood after examining Figure 4.14, it is a physical limitation of the system. The input is set to provide a maximum of 12 V. After the disturbance, the full range of the input is required in order to maintain the steady state temperature of 36 °C (resulting in steady state error of 4 °C). In order to compensate for this limitation, it would be required to use a power supply which can provide greater than 12 V inputs. Unfortunately, the heat transfer coefficient used for this simulation is an under-estimate of heat transfer coefficients

which would be experienced in operation of an airfoil (HTC for this study relates to 15 °C air moving at 8.62 m/s), so even greater voltage inputs would be required. By reducing the resistance of the sample, higher steady state temperatures are achieved, but also drawing greater current. In application of these heating elements, it would be required to carefully specify resistance in order to meet the power supply limitations of the application at hand. High voltages are not always available. High currents can generate excessive heat in connections and auxiliary wiring.

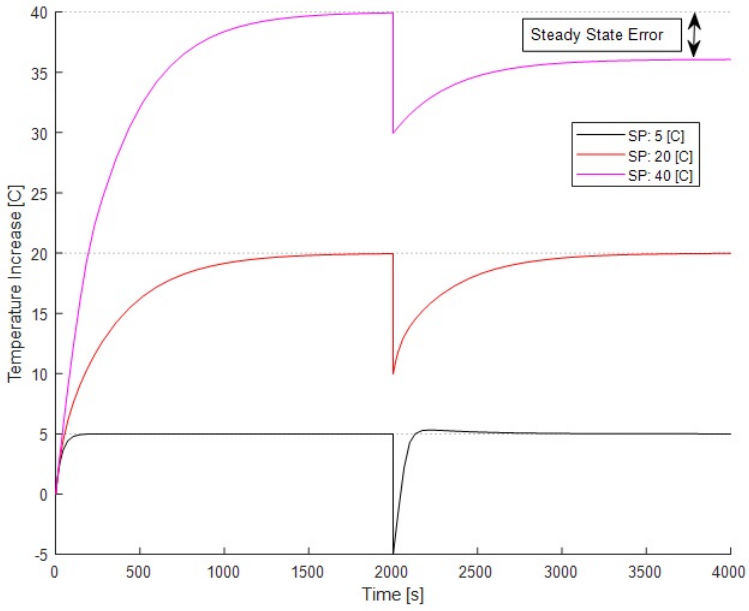

Figure 4.13: Temperature Response to Disturbance

Energy Consumption

Figure 4.16 shows that the integrator windup control saves 0.1, 7, and 16 kJ for the 5, 20, and 40 °C set point cases over the 4000 s experiment period respectively. At the cost rate of 0.0589 $\frac{\text{CAD}}{\text{kWh}}$ [53], 16 kJ is proportional to 0.26 μCAD. This is very small sum of money saved. But with extended operation and larger scale, this becomes more significant. The efficiency of this control system can be further improved with advanced control techniques. For systems such as automated flying machines, energy efficiency is an important consideration because of weight constraints.

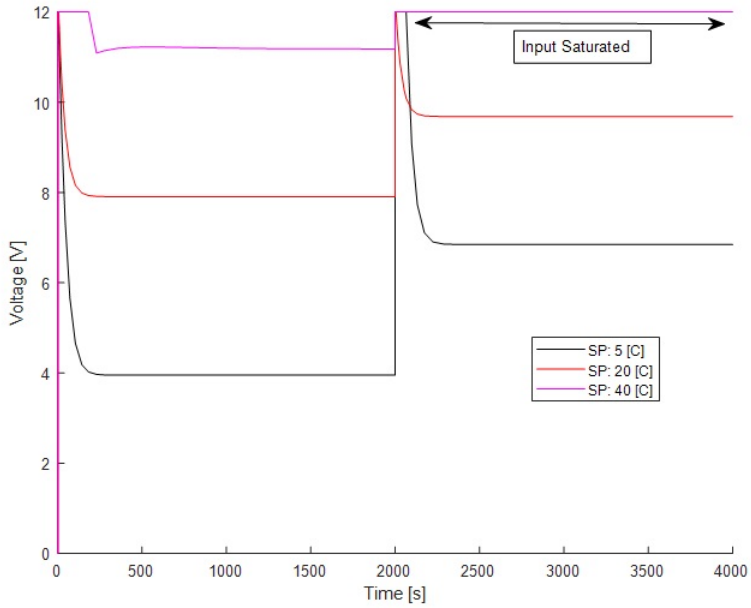

Figure 4.14: Voltage Input with Disturbance

The scale of the energy requirement of this heating system is understood by comparison to a standard phone battery. The 2020 model of a Google Pixel 3a XL has a charge capacity of 3.7 Ahr while supplying power at 4.3 V [54]. This translates to an energy capacity of 57.2 kJ. Without windup control this battery contains enough energy to power the heating element for 914, 2,055, and 8,140 s and with windup control it can power the element for 1,046, 2,055, and 8,119 s for set points of 40, 20, and 5 °C. In this case, windup control permits 14.4, 14.0, and 0.3 % longer operation until the battery capacity is depleted at 40, 20, and 5 °C set points. In a situation where an aerial vehicle's lift and drag coefficients are dependent on airfoil surface integrity, these longer operating times can be critical.

It is recognized that the results here are hypothetical. The transfer function used to generate these results was verified at 15 °C air temperature, while these predictions were made assuming required temperature increases of 40, 20, and 5 °C, thus air temperature of approximately -40, -20, and -5 °C. In application, the battery energy would deplete much sooner, since the heat flux between the surface and the air would

be larger than in this hypothetical case. This hypothetical case shows that more advanced control techniques would result in great efficiency of the heating system, and thus longer operating times for safe flight of aerial vehicles in icing conditions or greater power production from wind turbines in northern regions of the globe.

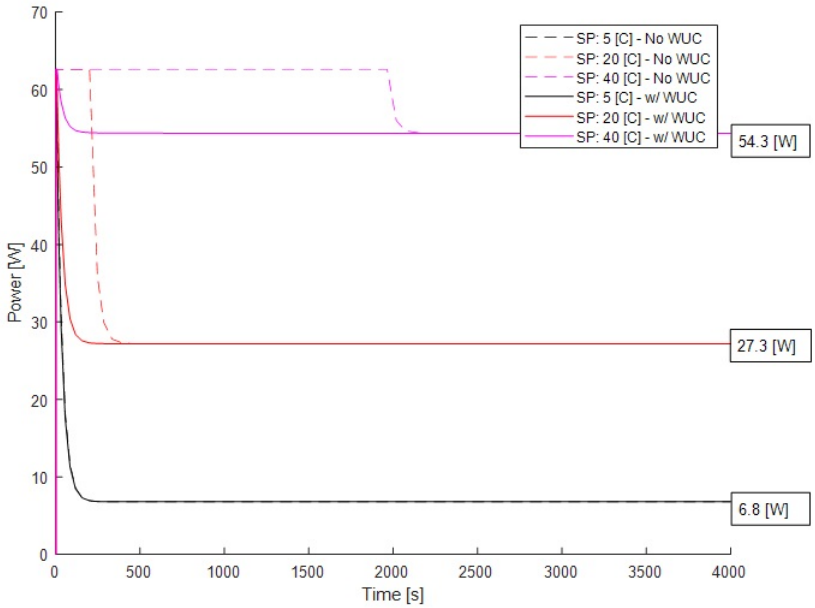

Figure 4.15: Power Draw by Heating Element

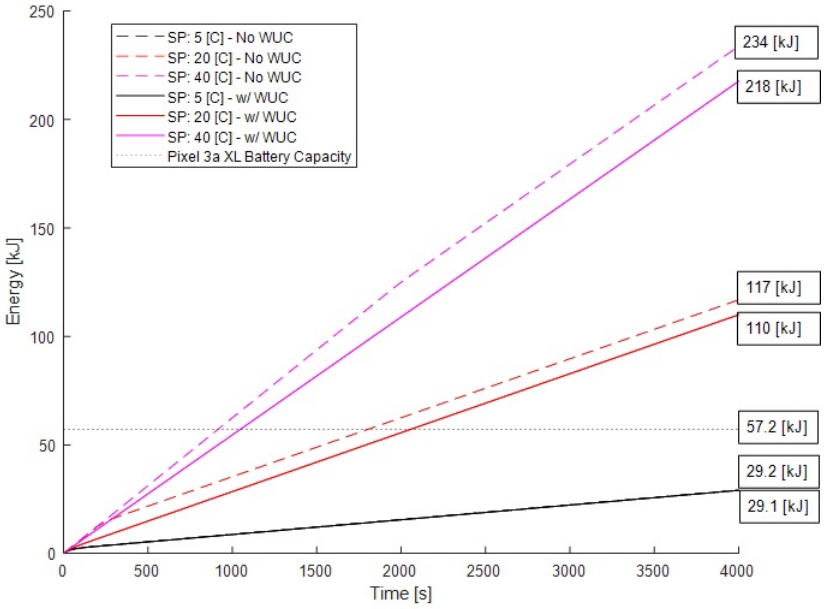

Figure 4.16: Energy Delivered to Heating Element

Chapter 5

Closing Statements

5.1 Conclusions

A first-order linear model describing the dynamical temperature response of a joule heating coating system manufactured with the flame spray process was derived, verified, and used to design a control system. A block of AISI 1018 steel was grit blasted, coated with Alumina, coated with NiCrAlY-Alumina 50 %/50 % to form the heating element, and the ends were cold sprayed with copper powder to form the power connections. The temperature response of the heating element was measured for 3, 6, and 9 V inputs under internal forced convection conditions at an air temperature set point of 15 °C. Time constant and zero-frequency gain were extracted from the data to verify model predictions and investigate the validity of the linear model in predicting the output. Heat transfer coefficient was determined experimentally and compared with that obtained via modeling. A sensor was designed, and used, to measure the resistance of coating as it heated up. The correlation from this study was inconclusive for any application, but shows experimentally that the resistance of the sample changed negligibly during the heating process. The first-order transfer function approximated the temperature increase for 6 V and 9 V inputs to 3.5 % and 3.9 %, this is accurate enough to be useful in designing a control system for regulating temperature of a joule heating element. For the lowest input (3 V) steady state temperature increase (2.4 °C) was predicted to 18.9 %, this error is a result of the 3.8 °C

temperature fluctuation range of the environmental air temperature inside the cold room. While the experimental system response did not exhibit significant non-linear behavior across the inputs tested, the HTC is non-linear with respect to fluid flow condition. This communicates that a linear model can be used to predict the system response accurately, provided that the designer of the system is confident in their prediction of HTC. This study shows how HTC can be predicted from the operation of the heating element, and suggests numerous methods to improve the control system. Designers can find application for the results of this work when looking to design a control system for regulating temperature using flame sprayed heating elements on any object, provided it can be coated using flame spray and the material properties are known.

5.2 Future Work and Recommendations

Resistance can be easily measured during operation of the heating element and HTC is difficult to predict accurately using regressions alone. It is recommended to design an observer of HTC, using resistance measurements. One approach to the design of this observer is to combine regression predictions of HTC, using a Kalman filter, with HTC predictions derived from resistance measurements.

HTC predictions can be made from temperature measurements using a method similar to the work in Section 4.3, improvements are required prior to implementation. The derived HTC should be used to update the linear model, this greater accuracy in the model permits greater efficiency of the control system as analyzed near the end of Section 4.7.

Change detection of the observed HTC state can be used to detect the presence of ice on the surface of the heating element, which can act as a signal to engage the deicing system. This was performed in [25] using the lift and drag coefficient parameters. Machine learning was used to analyze an ultrasonic signal transmitted through wind turbine blades in [28] to classify ice thickness.

Further, also using a Kalman filter the uncertainty in temperature predictions can be reduced by combining sensor measurements with model predictions. For this, sensor measurements could be from temperature sensors or measurements of resistance then correlated to average surface temperature similar to Equation (4.2) seen in Section 4.1.2. The designer of such a system is then posed with the problem of determining the resistance to temperature correlation for the object whose temperature is being controlled, under a general case. Machine learning can be applied to determine this relationship upon initialization of the system, using temporary temperature sensors on the surface of the heating element. Under the scenario described, it is beneficial to apply a thermal coating which exhibits a strong and linear relationship between resistance and temperature, while being robust to change from erosion, corrosion, or mechanical damage. Further still, the application of the Kalman filter would exhibit reduced noise relative to the signal produced from thermocouples, resulting in a better estimate for the observed HTC state for live updates to the linear model and for ice detection.

5.3 Requirement Specifications for Airfoil Deicing Systems Constructed with Flame Spray

RS 1: The deicing system should turn on automatically when ice forms, or ideally just prior to ice forming, on the surface of the airfoil. **Justification:** In order to not heat the surface unnecessarily.

RS 2: The control system should change temperature of the surface in such a way that minimum energy is used to achieve the set point. **Justification:** Energy available of aircraft is limited and the purpose of wind turbines is to produce power, not consume it.

RS 3: Sensors should be eliminated if possible. **Justification:** Sensors provide failure modes which can be critical for control systems.

RS 4: The heating element shall degrade negligibly as a result of erosion, corrosion, or mechanical damage. **Justification:** The heating element must be robust enough to maintain predictable operation.

RS 5: When deicing is engaged, all points on the surface of the heating element shall be at least 0 °C. **Justification:** Cold spots can result in ice buildup impairing the performance of the airfoil.

RS 6: The resistance of the deicing element shall be specified to meet the power supply constraints of the application. **Justification:** Low sample resistance results in a greater gain for the TF, but also results in greater current draw. Higher voltages can be applied to achieve heating, but are not necessarily available for the heating system. This requires consideration of the available power supply for the application at hand.

References

[1] M. B. Bragg, A. P. Broeren, and L. A. Blumenthal, "Iced-airfoil aerodynamics," *Prog. Aeronaut. Sci.*, vol. 41, no. 5, pp. 323–362, 2005.

[2] A. P. Broeren and M. B. Bragg, "Effect of airfoil geometry on performance with simulated intercycle ice accretions," *AIAA J. Aircr.*, vol. 41, no. 1, pp. 121–130, 2005.

[3] M. B. Bragg, A. Broeren, H. Addy, M. Potapczuk, D. Guffond, and E. Montreuil, "Airfoil ice-accretion aerodynamics simulation," *45th AIAA Aerospace Sciences Meeting and Exhibit, AIAA Paper No. 2007-0085*, 2007.

[4] B. Gulick, "Effects of simulated ice formation on the aerodynamic characteristics of an airfoil," *NACA Wr L-292*, 1938.

[5] T. Hu, H. Lv, B. Tian, and D. Su, "Choosing critical ice shapes on airfoil surface for the icing certification of aircraft," *Procedia Eng., 3rd ed.*, vol. 80, pp. 456–466, 2014.

[6] L. Dillingham, "Aviation safety: Preliminary information on aircraft icing and winter operations," *United States Government Accountability Office testimony before the subcommittee on aviation, Committee on Transportation and Infrastructure*, 2010.

[7] J. Cole and W. Sands, "Statistical study of aircraft icing accidents," *Fortieth aerospace science meeting and exhibit, AIAA-91-0558, Reno, Nevada, USA; January 7–10*, 1991.

[8] K. L. Sorensen and T. A. Johansen, "Flight test results for autonomous icing protection solution for small unmanned aircraft," *International Conference on Unmanned Aircraft Systems, ICUAS*, pp. 971–980, 2017.

[9] S. K. Thomas, R. P. Cassoni, and C. D. MacArthur, "Aircraft anti-icing and de-icing techniques and modeling," *J. Aircr.*, vol. 33, no. 5, pp. 841–854, 1996.

[10] S Barber, Y Wang, S Jafari, N Chokani, and R. S. Abhari, "The impact of ice formation on wind turbine performance and aerodynamics," *J. Sol. Energy Eng.*, vol. 133, no. 1, 2011.

[11] M. T. Brahimi, D. Chocron, and I. Paraschivoiu, "Prediction of ice accretion and performance degradation of hawt in cold climates," *1998 ASME Wind Energy Symposium*, vol. 26, no. 98, 1998.

[12] H. Seifert, A. Westerhellweg, and J. Kröning, "Risk analysis of ice throw from wind turbines," *Proc. of the BOREAS VI Conference, 9 to 13 April*, 2003.

[13] P. Frohboese and A.Anders, "Effects of icing on wind turbine fatigue loads," *J. Phys.: Conf. Ser. 75 012061*, 2007.

[14] *Density of dry air*, https://www.engineeringtoolbox.com/air-density-specific-weight-d_600.html, Accessed: 2020-05-05.

[15] *Density of wet air*, https://www.engineeringtoolbox.com/density-moist-air-_-1533.html, Accessed: 2020-05-05.

[16] *Polar and non-polar molecules*, http://www2.nau.edu/lrm22/lessons/polar_non-polar/polar_nonpolar.html, Accessed: 2020-05-05.

[17] M. B. Bragg, "Rime ice accretion and its effect on airfoil performance," Ph.D. dissertation, The Ohio State University, 1981.

[18] K. Kleissl and C. Georgakis, "Bridge ice accretion and de-and anti-icing systems: A review," in *The 7th Internation Cable Supported Bridge Operators' Conference*, 2010, pp. 161–167.

[19] O. Parent and A. Ilinca, "Anti-icing and de-icing techniques for wind turbines: Critical review," *Cold Reg. Sci. Technol.*, vol. 65, no. 1, pp. 88–96, 2011.

[20] R Hansman Jr, K. Breuer, D. Hazan, A. Reehorst, and M. Vargas, "Close-up analysis of aircraft ice accretion," in *31st Aerospace Sciences Meeting*, 1993, p. 29.

[21] G. Botura, D. Sweet, and D. Flosdorf, "Development and demonstration of low power electrothermal de-icing system," in *43rd AIAA Aerospace Sciences Meeting and Exhibit*, 2005, p. 1460.

[22] J Hille, "De-icing and anti-icing fluid residues," *Boeing Aero Magazine*, no. 25, pp. 15–21, 2007.

[23] S Farhadi, M Farzaneh, and S. Kulinich, "Anti-icing performance of superhydrophobic surfaces," *Appl. Surf. Sci.*, vol. 257, no. 14, pp. 6264–6269, 2011.

[24] *Boots deicing in severe icing conditions 2*, https://www.youtube.com, Accessed: 2020-05-05.

[25] K. L. Sørensen, "Autonomous icing protection solution for small unmanned aircraft: An icing detection, anti-icing and de-icing solution," Ph.D. dissertation, NTNU: Norwegian University of Science and Technology, 2016.

[26] K. L. Sørensen, A. S. Helland, and T. A. Johansen, "Carbon nanomaterial-based wing temperature control system for in-flight anti-icing and de-icing of unmanned aerial vehicles," in *2015 IEEE Aerospace Conference*, IEEE, 2015, pp. 1–6.

[27] J. Sabatier, P. Lanusse, B. Feytout, and S. Gracia, "Crone control based anti-icing/deicing system for wind turbine blades," *Control Eng. Pract.*, vol. 56, pp. 200–209, 2016.

[28] A. A. Jiménez, F. P. G. Márquez, V. B. Moraleda, and C. Q. G. Muñoz, "Linear and nonlinear features and machine learning for wind turbine blade ice detection and diagnosis," *J. Renewable Energy*, vol. 132, pp. 1034–1048, 2019.

[29] R. Aykan, C. Hajiyev, and F. Çalişkan, "Kalman filter and neural network-based icing identification applied to a340 aircraft dynamics," *Aircr. Eng.*, 2005.

[30] F. Caliskan, R. Aykan, and C. Hajiyev, "Aircraft icing detection, identification, and reconfigurable control based on kalman filtering and neural networks," *J. Aerosp. Eng.*, vol. 21, no. 2, pp. 51–60, 2008.

[31] D Michels, J Hadeler, and J. Lienhard V, "High-heat-flux resistance heaters from vps and hvof thermal spraying," *Exp. Heat Transfer*, vol. 11, no. 4, pp. 341–359, 1998.

[32] M. Prudenziati, "Development and the implementation of high-temperature reliable heaters in plasma spray technology," *J. Therm. Spray Technol.*, vol. 17, no. 2, pp. 234–243, 2008.

[33] A. Lopera-Valle and A. McDonald, "Application of flame-sprayed coatings as heating elements for polymer-based composite structures," *J. Therm. Spray Technol.*, vol. 24, no. 7, pp. 1289–1301, 2015.

[34] D. Tejero-Martin, M. R. Rad, A. McDonald, and T. Hussain, "Beyond traditional coatings: A review on thermal-sprayed functional and smart coatings," *Journal of Thermal Spray Technology*, vol. 28, no. 4, pp. 598–644, 2019.

[35] *Marketwatch article on thermal spray*, https://www.marketwatch.com/press-release/thermal-spray-material-market-analysis-2020-global-industry-details-size-share-overview-by-revenue-competitive-landscape-key-regions-and-forecast-to-2023-says-market-reports-world-2020-03-13, Accessed: 2020-06-05.

[36] Z. Zou, Y. Wang, F. Zhou, L. Wang, S. Liu, and Y. Wang, "Tribological property of plasma-sprayed al2o3-13wt% tio2 coatings onto resin-based composites," *Applied Surface Science*, vol. 431, pp. 75–80, 2018.

[37] M. R. Rad and A. McDonald, "Development of a thermal-sprayed coating system to mitigate ice accumulation and freezing damage in carbon steel pipes," *Proc. of the International Thermal Spray Conference*, vol. 2018-May, pp. 635–642, 2018.

[38] S. T. Dehaghani, A. Dolatabadi, and A. McDonald, "An experimental study of the performance of flame-sprayed ni-based metal matrix composite coatings as resistive heating elements," in *Proc. the International Thermal Spray Conference, Yokohama, Japan*, May 26–29 2019, pp. 527–534.

[39] J.-M. Lamarre, P. Marcoux, M. Perrault, R. C. Abbott, and J.-G. Legoux, "Performance analysis and modeling of thermally sprayed resistive heaters," *J. Therm. Spray Technol.*, vol. 22, no. 6, pp. 947–953, 2013.

[40] R. Gonzalez Henriquez, "Flame-sprayed al-12si coatings as damage detection sensors for fibre-reinforced polymer composites," 2015.

[41] J. Nicholls, N. J. Simms, W. Chan, and H. Evans, "Smart overlay coatings—concept and practice," *Surface and Coatings Technology*, vol. 149, no. 2-3, pp. 236–244, 2002.

[42] Y. Gao, J. Xiong, D. Gong, J. Li, and M. Ding, "Improvement of solar absorbing property of ni–mo based thermal spray coatings by laser surface treatment," *Vacuum*, vol. 121, pp. 64–69, 2015.

[43] *Engineering toolbox properties of steel*, https://www.engineeringtoolbox.com/thermal-conductivity-metals-d_858.html, Accessed: 2020-06-04.

[44] A. McDonald, B. Bschaden, E. Sullivan, and R. Marsden, "Mathematical simulation of the freezing time of water in small diameter pipes," *Appl. Therm. Eng.*, vol. 73, no. 1, pp. 142–153, 2014.

[45] *Kinematic and dynamic viscosity of air*, https://www.engineersedge.com/physics/viscosity_-of_air_dynamic_and_kinematic_14483.htm, Accessed: 2020-06-04.

[46] Y. Cengel and A. Ghajar, *Heat and mass transfer: fundamentals and applications*. McGraw-Hill Higher Education, 2014.

[47] *Thermal conductivity of air*, https://www.engineeringtoolbox.com/air-properties-viscosity-conductivity-heat-capacity-d_1509.html, Accessed: 2020-27-04.

[48] M. R. Rad and A. McDonald, "Mathematical simulation of heating and melting of solid ice in a carbon steel pipe coated with a resistive heating system," *Int. J. Heat Mass Transfer*, vol. 138, pp. 923–940, 2019.

[49] 2018.

[50] *Trace width calculator*, https://www.4pcb.com/trace-width-calculator.html, Accessed: 2020-06-04.

[51] *Coolterm softqare download*, https://freeware.the-meiers.org/, Accessed: 2020-06-04.

[52] G. F. Franklin, J. D. Powell, A. Emami-Naeini, and J. D. Powell, *Feedback control of dynamic systems*. Addison-Wesley Reading, MA, 1994, vol. 3.

[53] *Utilities consumer advocate*, https://www.ucahelps.alberta.ca/regulated-rates.aspx, Accessed: 2020-03-05.

[54] *Google cell phone products*, https://store.google.com/ca/product/pixel-3a-specs, Accessed: 2020-04-05.

Appendix A: Data Sheets

TECHNICAL DATA SHEET

FR-1 Printed Circuit Board

Physical Properties

Size	4x5″
Thickness	1.6mm
Copper Cladding	1 oz
Solder Resistance	20 Sec
Heat Resistance	130°C 30min
Peel Strength	2 kgf/cm

Flexural Strength Lengthwise	15 kgf/mm^2
Flexural Strength Crosswise	14 kgf/mm^2
Volume Resistivity	1.0×10^{12} Ω/cm
Surface Resistivity Adhesive Side	1.0×10^{11} Ω
Surface Resistivity Laminate Side	1.0×10^{10} Ω
Insulation Resistance	1.0×10^{1} Ω

Figure A.1: PCB Data Sheet

Appendix B: PCB Design Files

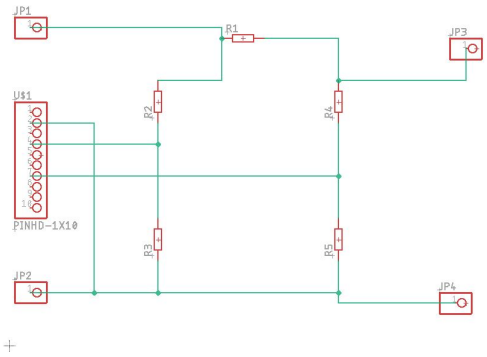

Figure B.1: Eagle PCB Component Layout

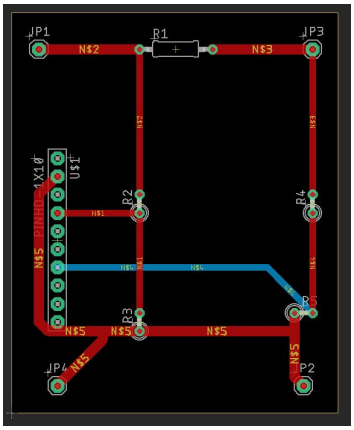

Figure B.2: Eagle PCB Tool Pathing

Property	Predicted Value	Measured Value	units	(Actual-Experimental)/Experimental
Sample Resistance	2.3056		Ohm	[%]
Voltage input	1		V	
Total current draw	0.30264	0.293	A	3.3
Voltage drop across shunt	0.30256	0.2967	V	2.0
Voltage at V2	0.69744	0.6903	V	1.0
Vsig1	0.16667	0.1633	V	2.1
Vsig2	0.11624	0.1155	V	0.6
Voltage input	3		V	
Total current draw	0.90792	0.889	A	2.1
Voltage drop across shunt	0.90767	0.8936	V	1.6
Voltage at V2	2.0923	2.0767	V	0.8
Vsig1	0.5	0.4921	V	1.6
Vsig2	0.34872	0.3476	V	0.3
Voltage input	6		V	
Total current draw	1.8158	1.783	A	1.8
Voltage drop across shunt	1.8153	1.79	V	1.4
Voltage at V2	4.1847	4.157	V	0.7
Vsig1	1	0.9841	V	1.6
Vsig2	0.69744	0.6931	V	0.6
Voltage input	9		V	
Total current draw	2.7238	2.676	A	1.8
Voltage drop across shunt	2.723	2.684	V	1.5
Voltage at V2	6.277	6.237	V	0.6
Vsig1	1.5	1.4757	V	1.6
Vsig2	1.0462	1.0437	V	0.2
Voltage input	10		V	
Total current draw	3.0264	2.974	A	1.8
Voltage drop across shunt	3.0256	2.983	V	1.4
Voltage at V2	6.9744	6.9337	V	0.6
Vsig1	1.6667	1.6394	V	1.7
Vsig2	1.1624	1.1583	V	0.4

Figure B.3: Voltage Divider Performance Testing

Appendix C: Control System Design

C.1 Simulink Block Diagram

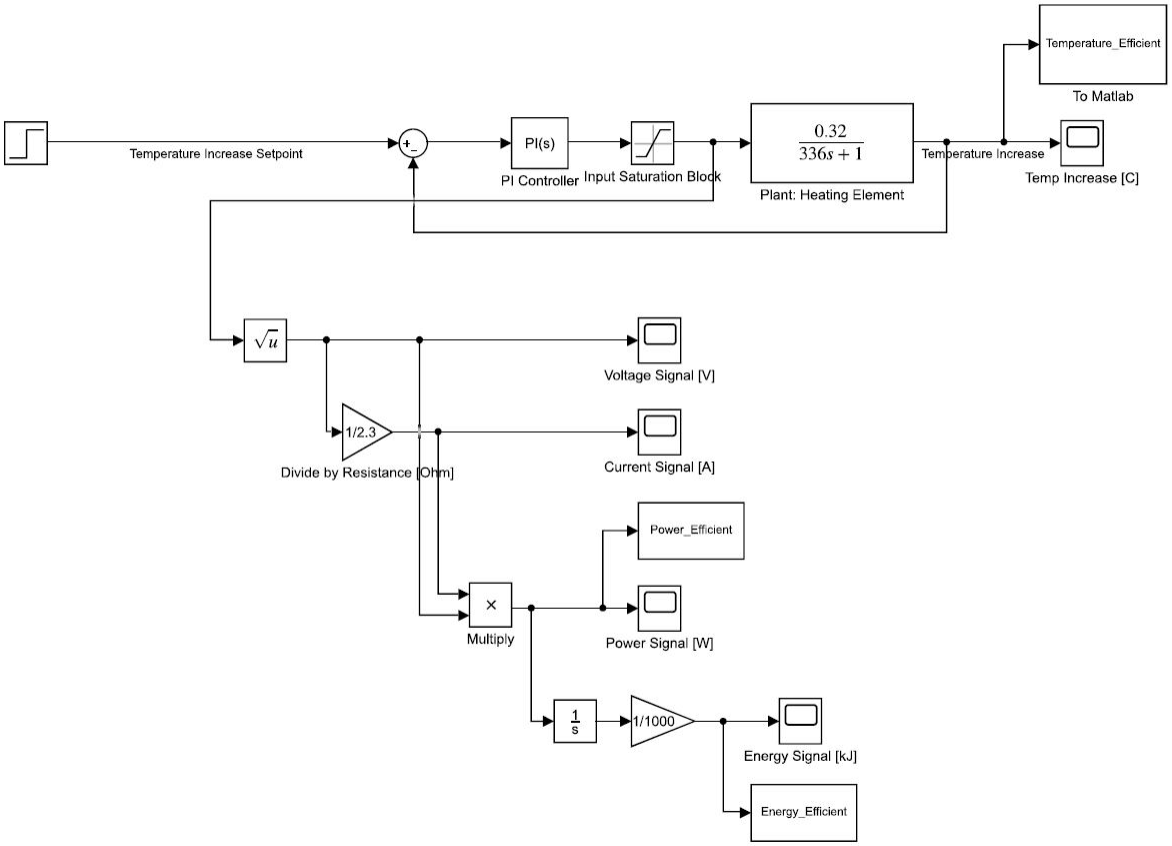

Figure C.1: Simulink Block Diagram

C.2 Tuner User Interface

1. Click PI block
2. Select tuning Method: Transfer Function Based (PID tuner App) from drop down menu
3. Click: tune...
4. Use slider bars at the top of the screen to change the gains of the PI block

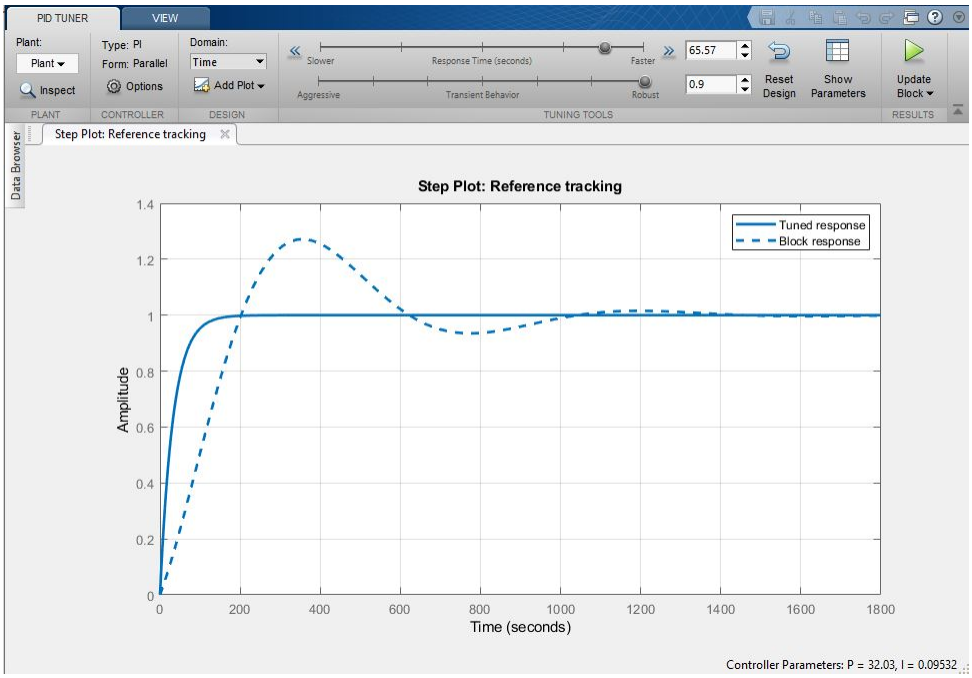

Figure C.2: Simulink PID Tuner User Interface

Appendix D: MATLAB® Code

D.1 Resistance Specification Code

Listing D.1: Resistance Specification

```
clc;
clear;

H=0.02;%m^2 - Thickness of Sample
c=486;%J/kgK - Heat Capacity of Steel Block
rho=7870;%kg/m^3 - Density of Steel Block
A=0.0069;%m^2 - Surface Area of sample Exposed to air
h=138; %W/m^2K - Heat Transfer Coefficient Which the sample is exposed to
Rcoating=1.8;% Ohm - Coating between copper terminals with flame sprayed
% resistive heating element acting as conductive pathway
V=3;%V - Voltage input to heating system


num=[1/(h*A*Rcoating)];
den=[rho*c*H/h 1];
sys=tf(num, den);
step(V^2*sys);
y=step(V^2*sys);
disp(['Steady State Temp: ', num2str(y(end))]);
```

D.2 Resistance to Temperature Correlation Code: Formatting, Filtering, Plotting, and Analysis

Listing D.2: Resistance to Temperature Correlation Code

```
clc;
clear;

load('TvsR.mat') %load previously formatted data file
Tdata=[S1 S2 S3 S4 S5 S6 Env1 Env2]; %format Temperature data into useful vector
Rdata=[V1 V2 I R]; %format Resistance Sensor data into useful vector
Rdata(29859:1:end, :)=[]; %Trim not useful data points from vector
Rdata(1:1:19, :)=[]; %Trim not useful data points from vector
Tdata(end, :)=[];
Tdata(:,9)=sum(Tdata(:,[1 2 3 4 5 6]), 2)/6; % average the temperature data

save('TvsR_TimeSynced.mat')
figure(1)
t=[1:1:length(Tdata)]';
t1=[1:1:length(Rdata)]';
title('Heating and Measuring Resistance');
hold on
yyaxis left
set(gca,'ycolor','b')
ylabel('Temperature [C]');
plot(t,Tdata(:,9), '-r');
plot(t,Tdata(:,7), '-b');
plot(t,Tdata(:,8), '-m');
yyaxis right
set(gca,'ycolor','k')
ylabel('Resistance [Ohm]');
plot(t1,Rdata(:,4), 'k');
hold off
grid on;
xlabel('Time [s]');
legend('Temperature - Bulk','Tenvironment - Channel',...
    'Tenvironment - Room','Resistance','Location','Best');

figure(2)
x=Rdata(:,4);
subplot(3,1,1);
plot(x);
ylabel('Temperature [C]');
xlabel('Time [s]');
title('Resistance Data - No Filtering');

L=10;
B = ones(1,L)/L; %numerator coefficients
A = [1]; %denominator coefficients
y1 = filtfilt(B,A,x); %filter input x and get result in y
y1(1:1:L)=[]; %Trim the filter results of end affects from moving average filter
subplot(3,1,2);
ylabel('Temperature [C]');
xlabel('Time [s]');
title('Resistance Data - 10 Point Average');
plot(y1);

L=100;
B = ones(1,L)/L; %numerator coefficients
y2 = filtfilt(B,A,x); %filter input x and get result in y
y2(1:1:L)=[]; %Trim the filter results of end affects from moving average filter
subplot(3,1,3);
ylabel('Temperature [C]');
xlabel('Time [s]');
title('Resistance Data - 100 Point Average');
```

```
plot(y2);
Tdata([1:1:L],:)=[];

figure(3)
t=[1:1:length(Tdata)]';
t1=[1:1:length(y2)]';
hold on
yyaxis left
set(gca,'ycolor','b')
ylabel('Temperature [C]');
plot(t,Tdata(:,9), '-r');
plot(t,Tdata(:,7), '-b');
plot(t,Tdata(:,8), '-m');
yyaxis right
set(gca,'ycolor','k')
ylabel('Resistance [Ohm]');
plot(t1,y2, 'k');
hold off
xlabel('Time [s]');
legend('Temperature - Bulk','Tenvironment - Channel',...
    'Tenvironment - Room','Resistance','Location','Best');

figure(4)
hold on
plot(x,'-k');
plot(y1,'-b');
plot(y2,'-m');
hold off
ylabel('Resistance [Ohm]');
xlabel('Time [s]');
legend('Unfiltered','Filtered - 10 Point Moving Average',...
    'Filtered - 100 Point Moving Average','Location','Best');

figure(5)
R_correlation=y2;
T_correlation=Tdata(:,9);
T_correlation((29740:1:end))=[]; ...
    % trimming the end of the data set in order to make vectors the same length
p = polyfit(T_correlation,R_correlation,3)
f1 = polyval(p,T_correlation);

hold on
plot(T_correlation, R_correlation);
plot(T_correlation, f1, '-k')
hold off
ylabel('Resistance [Ohm]');
xlabel('Temperature [C]');
legend('Resistance as a Function of Temperature',...
    '3rd Order Polynomial Fit','Location','Best');

p2=p*(40.6*5*10^-6)/12; %polynomials for resistivity
p3=p2*10^6; %polynomials for resistivity in terms of microns.
```

D.3 Sensitivity Study

Listing D.3: Sensitivity Study Code

```
clc;
clear;

H=2/100;%m
rho=7870;%kg/m^3 for AISI 1018 steel
c=486;%J/kgK for AISI 1018 steel
k=51.9;%W/mK for AISI 1018 steel
V=8.63;%m/s
H=2/100;%m
W=5/100; %width of sample
L=13.8/100;%length of sample
A=L*W; %Surface area of sample


%% specify HTC values for study
hnom=215;
hmax=250;
hmin=208;
h=ureal('h', 215,'Range',[208 250],'AutoSimplify','full');

%% secify R values for study
Rnom=2.3;
Rmax=Rnom*(1+0.023);
Rmin=Rnom*(1-0.023);
R=ureal('R',2.3,'Percentage',[-2.3 2.3],'AutoSimplify','off');

%% Uncertainty resulting from R
nummax=[1/(hnom*A*Rmax)];
nummin=[1/(hnom*A*Rmin)];
num=[1/(hnom*A*R)];
den=[rho*c*H/hnom 1];
Smax=tf(nummax, den);
Smin=tf(nummin, den);
S=tf(num, den);

% store max and min response values in order to change line width
[ymax,t1] = step(Smax*81);
[ymin,t2] = step(Smin*81);

figure(1)
hold on
plot(t1, squeeze(ymax),'-k', 'LineWidth',3)
plot(t2, squeeze(ymin),'-r', 'LineWidth',3)
step(S*81);
xlim([0 2500])
hold off
legend('Maximum Resistance','Minimum Resistance','Range of Uncertain Responses')
xlabel('Time [s]');
ylabel('Temperature Increase [C]');
title('');
display('Max SST1: ', num2str(ymax(end,1)));
display('Min SST2: ', num2str(ymin(end,1)));
%% Uncertainty resulting from HTC
nummax=[1/(hmax*A*Rnom)];
nummin=[1/(hmin*A*Rnom)];
num=[1/(h*A*Rnom)];
denmax=[rho*c*H/hmax 1];
denmin=[rho*c*H/hmin 1];
den=[rho*c*H/h 1];
Smax=tf(nummax, denmax);
Smin=tf(nummin, denmin);
S=tf(num, den);
```

```
% Store max and min response values in order to change line width
[ymax,t1] = step(Smax*81);
[ymin,t2] = step(Smin*81);

figure(2)
hold on
plot(t1, squeeze(ymax),'-k', 'LineWidth',3)
plot(t2, squeeze(ymin),'-r', 'LineWidth',3)
step(S*81);
xlim([0 2500])
hold off
legend('Maximum HTC','Minimum HTC','Range of Uncertain Responses')
xlabel('Time [s]');
ylabel('Temperature Increase [C]');
title('');
display('Max SST3: ',num2str(ymax(end,1)));
display('Min SST4: ',num2str(ymin(end,1)));
%% Uncertainty resulting from R and HTC
nummax=[1/(hmax*A*Rmax)];
nummin=[1/(hmin*A*Rmin)];
num=[1/(h*A*R)];
denmax=[rho*c*H/hmax 1];
denmin=[rho*c*H/hmin 1];
den=[rho*c*H/h 1];
Smax=tf(nummax, denmax);
Smin=tf(nummin, denmin);
S=tf(num, den);

% Store max and min response values in order to change line width
[ymax,t1] = step(Smax*81);
[ymin,t2] = step(Smin*81);

figure(3)
hold on
plot(t1, squeeze(ymax),'-k', 'LineWidth',3)
plot(t2, squeeze(ymin),'-r', 'LineWidth',3)
step(S*81);
xlim([0 2500])
hold off
legend('Maximum HTC and R','Minimum HTC and R','Range of Uncertain Responses')
xlabel('Time [s]');
ylabel('Temperature Increase [C]');
title('');
display('Max SST5: ',num2str(ymax(end,1)));
display('Min SST6: ',num2str(ymin(end,1)));
```

Sensitivity_Study.m

D.4 Set Point Tracking plots

Listing D.4: Set Point Tracking Plots

```
figure(1)
hold on
plot(Temperature_Efficient5,'--k')
plot(Temperature_Efficient20,'--r')
plot(Temperature_Efficient40,'--m')
plot(Temperature_Efficient5_2,'-k')
plot(Temperature_Efficient20_2,'-r')
plot(Temperature_Efficient40_2,'-m')
yline(5,':');
yline(20,':');
yline(40,':');
hold off
legend('SP: 5 [C] - No WUC','SP: 20 [C] - No WUC',...
    'SP: 40 [C] - No WUC','SP: 5 [C] - w/ WUC',...
    'SP: 20 [C] - w/ WUC','SP: 40 [C] - w/ WUC')
xlabel('Time [s]');
ylabel('Temperature Increase [C]');
title('');

figure(2)
hold on
plot(Power_Efficient5,'--k')
plot(Power_Efficient20,'--r')
plot(Power_Efficient40,'--m')
plot(Power_Efficient5_2,'-k')
plot(Power_Efficient20_2,'-r')
plot(Power_Efficient40_2,'-m')
hold off
legend('SP: 5 [C] - No WUC','SP: 20 [C] - No WUC',...
    'SP: 40 [C] - No WUC','SP: 5 [C] - w/ WUC',...
    'SP: 20 [C] - w/ WUC','SP: 40 [C] - w/ WUC')
xlabel('Time [s]');
ylabel('Power [W]');
title('');

figure(3)
hold on
plot(Energy_Efficient5,'--k')
plot(Energy_Efficient20,'--r')
plot(Energy_Efficient40,'--m')
plot(Energy_Efficient5_2,'-k')
plot(Energy_Efficient20_2,'-r')
plot(Energy_Efficient40_2,'-m')
hold off
legend('SP: 5 [C] - No WUC','SP: 20 [C] - No WUC',...
    'SP: 40 [C] - No WUC','SP: 5 [C] - w/ WUC',...
    'SP: 20 [C] - w/ WUC','SP: 40 [C] - w/ WUC')
xlabel('Time [s]');
ylabel('Energy [kJ]');
title('');

figure(4)
hold on
plot(Voltage_Efficient5,'--k')
plot(Voltage_Efficient20,'--r')
plot(Voltage_Efficient40,'--m')
plot(Voltage_Efficient5_2,'-k')
plot(Voltage_Efficient20_2,'-r')
plot(Voltage_Efficient40_2,'-m')
hold off
legend('SP: 5 [C] - No WUC','SP: 20 [C] - No WUC',...
    'SP: 40 [C] - No WUC','SP: 5 [C] - w/ WUC',...
    'SP: 20 [C] - w/ WUC','SP: 40 [C] - w/ WUC')
```

```
xlabel('Time [s]');
ylabel('Voltage [V]');
title('');
```